AMPK- and cGAS-Mediated Dual Sensing of Glucose and dsDNA Synergizes to Enhance Antitumor Immunity

Ruyuan Zhou[1,2,3,#], Jingyan Pei[1,3,#], Shasha Chen[4], Qin Shen[1,3], Qirou Wu[3,5], Shengduo Liu[2,3], Xin-Hua Feng[3,6], Jian Zou[7], Tingbo Liang[1,6], Y. Jessie Zhang[8], Sheng-Cai Lin[9], Penghong Song[1,*], Chen-Song Zhang[8,*], Qian Zhang[3,8,*], and Pinglong Xu[1,2,3,6,*]

[1] Department of Hepatobiliary and Pancreatic Surgery and Zhejiang Provincial Key Laboratory of Pancreatic Disease, The First Affiliated Hospital, School of Medicine, Zhejiang University, Hangzhou, 310058, China;

[2] Institute of Intellectual Medicine, ZJU-Hangzhou Global Scientific and Technological Innovation Center, Hangzhou, 310058, China;

[3] The MOE Key Laboratory of Biosystems Homeostasis & Protection and Zhejiang Provincial Key Laboratory of Cancer Molecular Cell Biology, Life Sciences Institute, Zhejiang University, Hangzhou, Zhejiang 310058, China;

[4] Zhejiang Provincial Key Laboratory for Water Environment and Marine Biological Resources Protection, College of Life and Environmental Science, Wenzhou University, Wenzhou 325035, China;

[5] Key Laboratory of Novel Targets and Drug Study for Neural Repair of Zhejiang Province, School of Medicine, Hangzhou City University, Hangzhou 310015, China

[6] Cancer Center, Zhejiang University, Hangzhou, Zhejiang 310058, China;

[7] Eye Center of the Second Affiliated Hospital School of Medicine, Institute of Genetics, School of Medicine, Zhejiang University, Hangzhou 310058, China;

[8] Department of Molecular Biosciences, University of Texas at Austin, Austin, TX 78712, USA;

[9] State Key Laboratory for Cellular Stress Biology, School of Life Sciences, Xiamen University, Xiamen, 361102, China;

[#] These authors contributed equally;

[*] Correspondence should be addressed to P.S., C.-S. Z., Q.Z., or P.X.

30 Address for correspondence:
31 Penghong Song
32 Department of Hepatobiliary and Pancreatic Surgery, The First Affiliated Hospital, School of
33 Medicine, Zhejiang University
34 79 Qingchun Road, Hangzhou 310003, China
35 E-mail: songpenghong@zju.edu.cn
36
37 Chen-Song Zhang
38 State Key Laboratory for Cellular Stress Biology, School of Life Sciences, Xiamen University,
39 Xiamen, Fujian, China
40 E-mail: cszhang@xmu.edu.cn
41
42 Qian Zhang
43 Department of Molecular Biosciences, University of Texas at Austin
44 100 E. 24th Street, Norman Hackerman Building (NHB) 4.130, Austin, TX 78712, USA
45 Tel: 1-512-471-1029
46 E-mail: qian.zhang1@austin.utexas.edu
47
48 Pinglong Xu
49 Life Sciences Institute, Zhejiang University
50 866 Yuhangtang Road, Nano Building, Room A555, Hangzhou, 310058, China
51 Tel: 86-571-88206078
52 E-mail: xupl@zju.edu.cn
53
54 **Running Title**: AMPK-TBK1 Integrates Glucose Availability to Antitumor Immunity

ABSTRACT

Intratumoral glucose availability is linked considerably to tumor growth, immune evasion, and metastasis. However, the precise molecular mechanisms by which glucose levels govern cellular and immune responses against tumors remain incompletely understood. Here, we explored the context of tumors of intersections between AMP-activated protein kinase (AMPK) and cGAS-STING signaling, a key pathway initiating antitumor immunity. We unexpectedly found that AMPK activation robustly enhances cGAS-STING signaling within cancer and immune cells, which potently impacts melanoma and colorectal cell senescence, organoid apoptosis, and the infiltration of $CD4^+$ and $CD8^+$ T lymphocytes. Using classic or newly developed AMPK agonist Aldometanib, $TBK1^{S511E/S511E}$ knock-in (KI) mice, glucose metabolic modulator, and AMPKα1/α2 dKO melanoma, we demonstrated that dual sensing of intratumoral glucose and dsDNA integrated by the AMPK-TBK1 cascade is essential for initiating antitumor immunity and suppressing cancer progressions. Notably, novel AMPK agonists or intervening in glucose glycolysis by Lonidamine synergized effectively with STING agonists, substantially inhibiting melanoma growth. Therefore, these findings unravel a concise mechanism integrating glucose metabolism and innate DNA sensing into cancer cell fate and propose an effective therapeutic strategy to enhance antitumor immunity.

Key Words: AMPK; TBK1; cGAS-STING; antitumor immunity; glucose metabolism; synergistic therapy; glucose sensing; nucleic acid sensing; AMPK agonists; senescence; apoptosis; dual sensing; T lymphocytes; melanoma; colorectal cancer; immunotherapy; immune evasion; glycolysis; tumor microenvironment; cancer immunology

77 **HIGHLIGHTS**

78 1. Dual and synergistic sensing of glucose and dsDNA facilitates antitumor immunity in
79 melanoma and colorectal cancer;
80 2. AMPK substitutes intratumoral cGAS-STING-IRF3 signaling through TBK1
81 phosphorylation at S511;
82 3. Glucose deficiency induces cancer cell senescence, apoptosis, and T lymphocyte
83 infiltration via the AMPK-TBK1 cascade;
84 4. Newly developed AMPK agonists synergize with STING agonists to retrieve striking
85 tumor suppression.
86
87

88 **INTRODUCTION**

89 Nucleic acid sensing surveils tissue abnormalities and pathogen invasion and establishes an
90 immune state to restrict microbial infection, modulate adaptive immunity, and guide tissue
91 repair and regeneration [7-11]. Pattern recognition receptors (PRRs) such as cGAS [12,13] monitor
92 microbes and tissue damage by perceiving cytosolic dsDNA derived from pathogens, the
93 mitochondria, or the nucleus [7,8,10,14]. Upon recognition of free dsDNA, cGAS synthesizes 2'3'-
94 cyclic GMP-AMP (cGAMP)[12,15-17], activates STING (also known as MITA or ERIS) [18-20], which
95 triggers the non-canonical STING-PERK pathway in the endoplasmic reticulum (ER) that
96 regulates mRNA translation [21], induces non-canonical autophagy in the ERGIC [22], and
97 facilitates the activation of TBK1 and IRF3 at the Golgi apparatus [23,24]. Phosphorylated IRF3
98 translocates into nuclear and transcribes type I interferons (IFN-Is) and numerous IFN-
99 stimulated genes (ISGs) [25,26], in coordination with simultaneously activated NF-κB [7,8,10].
100 Therefore, nucleic acid sensing induces mRNA translation arrest [21], autophagy [22,27,28], phase
101 separation [29], mitochondrial dynamics [30], cell differentiation [31], and triggers cell senescence
102 [32-35] and cell death [36-38].

103 Effects of cGAS-STING signaling in tumor biology are complex and multifaceted [39]. cGAS-
104 STING signaling is active in cancerous, immune, and stromal cells, shifting their cellular
105 function, metabolism, and fate. The activation of cGAS-STING signaling releases various IFN-I,
106 cytokines, cGAMP, and DNA, which attracts and matures dendritic cells, macrophages, natural
107 killer cells (NKs), and effector T lymphocytes to mount an antitumor immunity [40,41]. STING-
108 induced senescence and immune microenvironment modulation also participate in antitumor
109 immunity regulation, positively or negatively [42,43,44,45,46,47], and STING-dependent residency of
110 tumor-associated macrophages (TAMs) attenuate its antitumor role [48]. Therefore, the effects
111 of cGAS-STING in cancer biology could be context- and stage-dependent and should be
112 carefully evaluated during cancer treatments.

113 Cells in multicellular organisms depend on balanced nutrient availability for survival,
114 growth, and defense. Despite this, the direct molecular connection between nutrient sensing
115 and tissue damage perception remains less understood. AMP-activated protein kinase (AMPK)
116 plays a central role in detecting glucose deficiency and controlling metabolic pathways [49-51].
117 AMPK is activated at the lysosomal surface in response to low glucose levels through aldolase

118 and the v-ATPase-Ragulator complex[52-54], in addition to being induced by AMP/ATP ratios and
119 kinase such as LKB1 or CaMKII [50,55,56]. AMPK masterly regulates an array of cellular processes
120 such as glucose and lipid metabolism, protein synthesis, autophagy, mitochondrial biogenesis,
121 and overall metabolism [50,57], and its dysfunction is broadly accompanied by obesity, type 2
122 diabetes, and cancers. We recently reported that viral infection causes a rapid and dramatic
123 decrease in blood glucose levels and substantially activates AMPK in tissues, which directly
124 phosphorylates TBK1 to trigger IRF3 recruitment and assemble MAVS or STING signalosomes,
125 thus effectively mounting antiviral immunity[2]. In adipocytes, TBK1 also represses energy
126 expenditure by inhibiting AMPKα [58]. These observations indicate the presence of the
127 intersection between metabolic master kinase AMPK and immune key kinase TBK1.
128 Nevertheless, the roles of metabolism and immunity crosstalk through AMPK-TBK1 signaling
129 in the context of malignant diseases remain poorly understood.
130 However, hyperglycemia has been considerably linked to diabetes-related vulnerability to
131 malignancy [59], and it impacts cancer immunology in distinct ways. For instance, elevated
132 glucose levels through the hexosamine biosynthesis pathway (HBP) enhance the O-
133 GlcNAcylation level in TAMs, promoting M2-like polarization and cancer progression [60]. In diet-
134 induced obesity, more immunosuppressive myeloid-derived suppressor cells (MDSCs) were
135 observed with higher tumor progression of pancreatic cancer [61,62]. Meanwhile, tumor cells
136 typically exhibit increased glucose uptake and enhanced glycolysis, which supports key
137 processes for tumorigenesis, such as the biosynthesis of nucleotides, amino acids, and lipids.
138 Focusing on the AMPK-TBK1 axis, here we systematically investigated the link between
139 glucose availability and antitumor immunity. Using the well-documented and newly
140 developed AMPK agonists and TBK1 S511E knock-in (KI) mice, we found that activated AMPK
141 directly phosphorylated intratumoral TBK1 at S511, promoting cGAS-STING-initiated
142 senescence and antitumor immunity, thereby attenuates the progression of melanoma and
143 colorectal cancer. In summary, we proposed an intratumoral dual and synergistic sensing of
144 dsDNA and glucose, which forms a "metabolism and immune sensing" bridge through the
145 concise AMPK-TBK1 signaling and determines tumor progression.
146

147 **RESULTS**

148 **Glucose deficiency promotes intratumoral cGAS-STING signaling**

149 To explore the function of glucose metabolism on antitumor immunity in TME, we investigated
150 the state of glucose deficiency and its impacts on cGAS-STING signaling, an innate immune
151 pathway crucial in antitumor immunity. Intratumoral glucose deficiency was evident, as
152 reported [63-65], and as indicated by AMPK-induced phosphorylation of metabolic regulator
153 ACC1 in melanoma (Fig. 1A-1B). pACC1 signal was particularly robust at tumor edges, where
154 proliferating tumor cells and immune cells need high glucose demand. cGAMP treatment in
155 primary peritoneal macrophages (PMs) triggered robust activation of TBK1 and IRF3, the
156 central kinase and key signaling mediator of cGAS-STING signaling. Simulating an intratumoral
157 glucose-depleted microenvironment using 2-deoxy-D-glucose (2-DG) resulted in an enhanced
158 cGAS-STING-IRF3 pathway when compared to energy-sufficient conditions, accompanied by
159 robust activation of AMPK (Fig. 1C). We observed a similar enhancement of cGAS-STING
160 signaling in colorectal adenocarcinoma cells (DLD1) and mouse embryonic fibroblasts (MEFs)
161 under energy-deficient conditions (Figs. 1D-1E). AICAR, a well-established AMPK agonist [66],
162 expectedly facilitated cGAS-STING signaling in fibroblasts and cancer cells (Figs. 1D-1E).
163 Likewise, glucose depletion amplified mitochondrial DNA (mtDNA)-induced activation of
164 cGAS-STING-IRF3 signaling in colorectal carcinoma cells (Fig. 1F), achieved by combinational
165 treatment of ABT-737, qVD-OPH, and S63845 (AQS) [67-69]. AICAR also potentiated the sensing
166 of cytosolically exposed dsDNA in DLD-1 cells, simulated by poly(dA:dT) transfection (TpdAdT)
167 (Fig. 1G). These observations across immune cells, fibroblasts, and cancer cells suggest that
168 glucose deficiency, frequently seen in tumors, significantly augments cGAS-STING signaling
169 and is likely through AMPK activation.

170

171 **AMPK facilitates cGAS-STING signaling in cancer cells by TBK1 S511 phosphorylation**

172 To validate that glucose deficiency regulates nucleic acid sensing through AMPK activation, we
173 generated AMPK α1/α2 dKO cells in B16-F10 melanoma cells using a CRISPR-mediated
174 approach (Fig. 2A). Genetic deletion of AMPK catalytic subunits α1/α2 attenuated cGAS-
175 STING-IRF3 signaling in B16 melanoma, as indicated by reduced levels of phospho-STING
176 (S366) and phospho-IRF3 (S396) (Fig. 2A). Likewise, deletion of AMPK α1 and α2 subunits in

177 colorectal carcinoma HCT116 cells similarly decreased RLR-MAVS-IRF3 signaling (Fig. 2B), the
178 dsRNA pathway with an emerged role in antitumor immunity [70,71]. The role of AMPK on TBK1
179 activation was also evident as AMPK catalytic subunits strongly potentiated the TBK1-IRF3
180 interaction (Fig. 2C) and TBK1-stimulated IRF3 transactivation (Fig. 2D). Our previous study
181 and the mass spectrometry analyses of AMPK-coexpressed TBK1 have identified that the S511
182 residue on TBK1 is abundantly modified by AMPKα1 [2]. We found that AMPK inhibitor
183 dorsomorphin (Compound C) abolished TBK1 S511 phosphorylation (Fig. 2E), and an antibody
184 specifically recognizing phospho-TBK1 S511 demonstrated that AMPKα1 directly
185 phosphorylated TBK1 at this residue (Fig. 2F). We thus evaluated the capability of wild-type,
186 phospho-resistant (S511A), and phosphomimetic TBK1 (S511E) to activate IRF3 by an IRF3-
187 responsive reporter, which indicated that AMPK-mediated TBK1 phosphorylation at S511 was
188 critical for driving IRF3 transactivation (Fig. 2G). Expectedly, a compromised interaction
189 between phospho-resistant TBK1 and IRF3 was seen (Fig. 2H). These findings suggest that
190 AMPK enhances cGAS-STING signaling by phosphorylating TBK1 at S511 to prime TBK1
191 activation.

192 To validate this AMPK-TBK1 axis in cancer cells, we generated and examined knock-in (KI)
193 clones of colorectal cells DLD1 with mutations that either prevent (S511A) or mimic (S511D)
194 AMPK-mediated modification by CRISPR-based genome editing [2]. cGAS-STING signaling was
195 attenuated when endogenous TBK1 was mutated into the S511A variant that resists AMPK
196 modification (Fig. 2I). Conversely, STING signaling was robustly activated when endogenous
197 TBK1 was mutated to the S511D variant that mimics AMPK-TBK1 phosphorylation, to a level
198 comparable to those under AICAR treatment (Fig. 2J). Noticeably, the AICAR-enhanced
199 activation of STING signaling was absent in these DLD1 KI cells (Fig. 2J). These observations
200 suggest that AMPK-mediated TBK1 phosphorylation at residue S511 is critical for cancer cells
201 to respond to glucose deficiency.

202

203 **AMPK drives STING-induced cancer cell senescence and apoptosis**

204 cGAS-STING responds to dsDNA leakage and drives cellular senescence, which could be
205 important in tumor growth arrest [32-34]. We found that upon chemical induction of DNA
206 damage, colorectal carcinoma DLD1 cells displayed strong phenotypes of cellular senescence,

207 evidenced by SA-β-Gal staining and senescence-associated secretory phenotypes (SASPs) (Fig.
208 3A-3B). Genetic ablation of AMPK α1/α2 subunits endowed DLD1 with apparent resistance to
209 DNA damage-induced cellular senescence (Fig. 3A). By contrast, AICAR facilitated the
210 progression of these colorectal cancer cells into senescence (Fig. 3B). In agreement with these
211 observations, simulating the glucose-depleted microenvironment using 2-DG greatly
212 enhanced DLD1 senescence (Fig. 3C). We further found that by utilizing a zebrafish model of
213 damage-induced senescence, AMPK activation by AICAR promoted camptothecin (CPT)-
214 induced senescence in zebrafish, indicated by increased numbers of SA-β-Gal-positive cells in
215 the heads and tails of zebrafish (Fig. 3D). Inhibition of AMPK by dorsomorphin strongly
216 attenuated CPT-induced senescence, as expected (Fig. 3D). These observations suggest that
217 AMPK is critical to regulate damage-induced cellular senescence, mediated by cGAS-STING
218 signaling.
219 The activation of cytosolic dsDNA sensing also mediates a context-dependent apoptotic
220 program [72], an evolved strategy beneficial to tissue homeostasis. We found that activation of
221 cGAS-STING by DNA damage inducer HU [73] triggered significant levels of colorectal cancer cell
222 apoptosis, which was noticeably regulated by AICAR and dorsomorphin (Fig. 3E). Additionally,
223 by utilizing *in vitro*-cultured intestinal organoids, we detected a strong phenotype of HU-
224 induced apoptosis among intestinal cells, which was further exaggerated by AMPK activation
225 (Fig. 3F). These observations suggest that glucose deficiency and resulting AMPK activation
226 controls both senescence and apoptosis of cancer and functional cells through an AMPK-TBK1
227 axis.
228
229 **AMPK-TBK1 signaling facilitates STING-mediated antitumor immunity in melanomas**
230 Next, we utilized a naturally occurring and constitutively active STING SAVI mutant (R281Q) to
231 generate B16-F10 melanoma with inducible and constitutively active STING signaling. Upon
232 implanting subcutaneously into wild-type C57BL/6 mice, we found that melanomas harboring
233 STING R281Q SAVI mutation exhibited significantly reduced growth (Figs. 4A-4C), attributed
234 mainly from STING-induced expression of type I interferons (IFNs) [73]. Increased immune cells
235 infiltrated these melanomas with constitutive STING signaling, particularly T cells (Figs. 4D-
236 4E), indicating enhanced antitumor immunity. Administration of AMPK agonist AICAR

237 significantly intensified T lymphocyte infiltration in melanomas (Figs. 4D-4E) and suppressed
238 tumor growth substantially (Figs. 4A-4C), suggesting that AMPK can amplify STING-mediated
239 antitumor immunity in melanoma.

240 To determine whether the AMPK-TBK1 axis mediates this enhanced antitumor immunity
241 effects, we generated knock-in (KI) mice harboring the TBK1 S511E mutation using a CRISPR-
242 mediated strategy [2], which mimics AMPK-mediated TBK1 phosphorylation. The TBK1 S511E
243 homozygous mice were viable, fertile, and appeared phenotypically normal. However,
244 melanoma growth was markedly attenuated in these TBK1 S511E mice (Figs. 4F-4H), along
245 with a significantly increased level of T lymphocyte infiltration (Figs. 4I-4J). More elevated
246 antitumor immunity was not seen in TBK1 S511E knock-in mice in the presence of cGAMP
247 (Figs. 4F-4H), further suggesting the importance of AMPK-TBK1 signaling in this process. These
248 consistent observations propose the AMPK-TBK1 axis as a critical factor in facilitating STING-
249 mediated antitumor immunity.

250

251 **AMPK agonists synergize well with cGAMP to promote antitumor immunity in melanomas**

252 To evaluate the potential for improving intratumoral antitumor immunity through this AMPK-
253 TBK1 axis, we employed in the in vivo model of melanoma a well-characterized AMPK agonist
254 AICAR [66] and a newly developed AMPK agonist Aldometanib [54], which acts through distinct
255 mechanisms. As expected, administration of cGAMP in mice, a natural STING ligand, resulted
256 in significant tumor growth suppression. AICAR (Figs. 5A-5C) and Aldometanib (Figs. 5D-F)
257 markedly enhanced melanoma growth arrest, synergizing well with cGAMP. These findings
258 suggest that maneuvering AMPK activation can effectively strengthen STING-induced
259 antitumor immunity. Intriguingly, we observed that Aldometanib also enhanced antitumor
260 effects in mice bearing AMPK dKO B16-F10 melanomas (Figs. 5G-5I), suggesting an additional
261 cancer cell-nonautonomous effect of Aldometanib in melanoma.

262

263 **Interrupting aerobic glycolysis potentiates antitumor immunity through the AMPK-TBK1**
264 **cascade**

265 Next, we interrupted glucose metabolism by inhibiting aerobic glycolysis in cancer cells using
266 Lonidamine, a classical hexokinase inhibitor [74], to evaluate the potential of glucose

267 metabolism intervention in antitumor immunity. Lonidamine interferes with energy
268 metabolism and induces AMPK activation [53,75,76]. Notably, we found that combinational use of
269 cGAMP and Lonidamine resulted in substantial tumor growth arrest (Figs. 6A-6C), along with
270 significantly increased infiltration of intratumoral T lymphocytes in melanomas (Figs. 6D-6E).
271 Furthermore, we found that Lonidamine promoted the robust activation of intratumoral
272 cGAMP-induced cGAS-STING signaling, evidenced clearly by increased levels of
273 phosphorylated STING (pSTING S365), STING clustering, and phosphorylated TBK1 (pTBK1
274 S172) in B16-F10 melanomas (Fig. 6F). These findings suggest that targeting glucose
275 metabolism can be a promising strategy in antitumor therapeutic, such as in melanomas.
276

277 **DISCUSSION**

278 Tumor cell metabolism depletes essential nutrients in the tumor microenvironment (TME),
279 leading to significant glucose competition between cancer and immune cells. Meanwhile, the
280 intervention of cGAS-STING signaling is a significant feature of cancers, mainly by genetic
281 deletion of signaling components and suppression of signaling cascades, which attenuates its
282 beneficial roles in antitumor immunity [29,73,77]. However, the exact mechanisms for cGAS-STING
283 activation and its contribution to cellular behaviors in cancer and immune cells, such as cell
284 death, senescence, IFN secretion, and metabolic changes, need further interrogation. This
285 study elucidated how the glucose sensor AMPK senses intratumoral glucose abundance and
286 promotes antitumor immunity through direct phosphorylation and activation of TBK1, an
287 essential kinase during innate immune responses. Given the complex energy metabolism in
288 TME, understanding the AMPK-TBK1 axis opens new avenues for targeting glucose
289 metabolism in both cancer and immune cells. Through activating cGAS-STING signaling and
290 enhancing T-cell-mediated antitumor immunity, these findings provide significant therapeutic
291 targets for drug development in cancer immunotherapy.

292 Cancer cells primarily rely on aerobic glycolysis for energy metabolism, through which
293 glucose is converted into lactic acid. This metabolic shift exacerbates glucose deficiency stress
294 within the tumor, leading to metabolic competition between tumor cells and immune cells.
295 Notably, these metabolic changes in immune cells contribute to establishing an
296 immunosuppressive microenvironment for accelerating tumor growth and immune evasion.
297 While previous studies have extensively characterized the Warburg effect and its impact on
298 tumor proliferation and immune suppression, this study focuses on how metabolic sensing
299 mechanisms combined with nucleic acid sensing influence the immune landscape of the TME.
300 The cGAS-STING pathway facilitates immune cell recruitment and inhibits tumor progression
301 through cellular senescence and apoptosis [42]. A recent study has highlighted that the AMPK-
302 TBK1 axis plays a crucial role in innate antiviral immunity, extending AMPK's function beyond
303 its classical roles in glucose and lipid metabolism, protein synthesis, autophagy, and
304 mitochondrial function [2]. Changes in glucose metabolism in the TME are closely linked to
305 immune responses. We found that the interaction between AMPK and cGAS-STING forms a
306 "metabolic and immune sensing" bridge, which synergistically senses the metabolic state of

307 tumor cells and tumor microenvironment to decide the magnitude of immune responses
308 during tumorigenesis. AMPK directly phosphorylates S511 residue on TBK1, enhancing STING-
309 IRF3 signaling activation and promoting T-cell infiltration into the TME, significantly inhibiting
310 melanoma growth. Therefore, these findings expand the understanding of metabolic
311 integration in innate immunity and provide new insights into antitumor immunity.

312 New therapeutics for tumor treatment increasingly focus on regulating cellular
313 metabolism and immune responses. We propose that modulating glucose levels within
314 tumors, the activation state of AMPK, and the modulation of AMPK-TBK1 signaling could offer
315 novel aspects for antitumor therapeutics. As a critical energy sensor, AMPK is activated in
316 response to glucose deprivation, thereby adjusting the cellular metabolic state. Our study
317 revealed that AMPK activation leads to direct phosphorylation of TBK1 at S511, enhancing
318 cGAS-STING-IRF3 signaling and promoting antitumor immune responses and STING-induced
319 cellular senescence and apoptosis, thereby potently inhibiting tumor growth. Besides, AMPK
320 plays an important role in the adaptive stress response of tumor cells, regulating key
321 metabolic pathways to inhibit tumor cell proliferation [51]. We supposed AMPK also influences
322 the metabolism of immune cells in the TME, particularly macrophage polarization, which
323 impacts tumor immune evasion. By modulating AMPK activity, immune cell surveillance of
324 tumors can be enhanced through cGAS-STING signaling, effectively preventing tumor immune
325 escape.

326 In conclusion, our study reveals the key role of the concise AMPK-TBK1 axis in regulating
327 intratumoral glucose metabolism and promoting antitumor immune responses, which
328 considerably connects glucose metabolism with innate immunity. We propose that targeting
329 the AMPK-TBK1 axis, the intersection between intratumoral glucose metabolism and
330 antitumor immunity, could reach a substantial synergy for cancer treatments.

331

332

ACKNOWLEDGMENTS

This research was sponsored by the NSFC Projects (32321002, 32430028, and 31830052 to P.X., 82271768 to Q.Z., and 82001668, 32370759 to S.C.) and the National Key Research and Development Program of China (2021YFA1301401 to P.X. and 2021YFD1801103 to Q.Z.). Thanks also to technical assistance by the Life Sciences Institute core facilities, Zhejiang University.

AUTHOR CONTRIBUTIONS

Q.Z. and R.Z. carried out most experiments. C.-S.Z., J.P., S.C., Q.S., Q.W., and S.L. contributed to several experiments. X.-H.F., J.Z., T.L., Y.J.Z., S.-C.L., P.S., and C.-S.Z. helped with reagents, data analyses, and discussions. P.X., Q.Z., and R.Z. conceived the study and experimental design and wrote the manuscript.

COMPETING FINANCIAL INTERESTS

The authors declare no competing financial interests.

349 **MATERIALS AND METHODS**

350 **Mice**

351 TBK1 S511E transgenic mice were on C57BL/6 background, and both male and female
352 littermates were used in all the experiments. GemPharmatech generated TBK1 Knock-in
353 transgenic C57BL/6 mice. To create point mutations (S511E) at mouse Tbk1 locus by
354 CRISPR/Cas9-mediated genome engineering, Tbk1 S511E (TCT to GAA) specific sgRNA oligos
355 were designed by the CRISPR website (http://crispr.mit.edu/) targeting sequence at S511
356 locus (5'- TTCTATTGTTCCCTGAGAAC -3') and (5'- ATTTAGCTTTCCAGTTCTCA -3'), with S511E
357 oligo donor sequence (5'-
358 CATTTGGATCTGATCCGTTGTTCTGACCTAACCTAACCCGTTGTATTTAGCTTTCCAGCGAACAGGGAAC
359 AATAGAAAGCAGTCTTCAGGACATCAGCAGCAGGCTGTCTCCAGGGGGCT -3'). Cas9 mRNA and
360 sgRNA generated by in vitro transcription and donor oligo were co-injected into fertilized eggs
361 for knock-in mouse production. The target region of the mouse Tbk1 locus was sequenced to
362 confirm targeting. All the animals were bred and maintained in a pathogen-free animal facility
363 at the laboratory animal center of Zhejiang University. The care of experimental animals was
364 approved by the Zhejiang University committee and followed Zhejiang University guidelines.

365 **Zebrafish**

366 Zebrafish AB wild-type embryos (male/female) were raised at 28.5°C in E3 egg water. The care
367 of experimental animals was approved by the Zhejiang University committee and followed
368 Zhejiang University guidelines.

369 **Peritoneal Macrophages**

370 Peritoneal macrophages were isolated from C57BL/6 mice at 6-8 weeks of age with the Brewer
371 thioglycollate medium (Sigma-Aldrich)-induced approach. Three days after the intraperitoneal
372 injection of 2.5 mL of 3% thioglycollate medium, peritoneal macrophages were isolated and
373 cultured in the RPMI 1640 medium.

374 **Cell Lines**

375 HEK293, HCT116, DLD1, MEFs, and B16-F10 cells were from ATCC. No cell lines used in this
376 study were found in the database of commonly misidentified cell lines maintained by ICLAC

377 and NCBI Biosample. Cell lines were frequently checked in morphology under microscopy and
378 tested for mycoplasma contamination but were not authenticated. All cell lines were cultured
379 in DMEM medium with 10% fetal bovine serum (FBS) at 37°C in 5% CO_2 (v/v), except for
380 peritoneal macrophages that were maintained in RPMI 1640 medium,

381 **Intestinal Organoids**

382 Isolated small intestines were opened longitudinally, washed three times with cold PBS,
383 removed the villi by scraping, and incubated twice in cold PBS with 2 mM EDTA for 15 min on
384 ice. After removing the EDTA medium, the fractions were incubated in 50 mL cold PBS with a
385 fierce shake and passed through a 70-µm cell strainer (BD Bioscience) to remove the residual
386 villous material. Isolated crypts were centrifuged at 300 g for 5 min to separate the crypts with
387 single cells. The centrifuged fractions were suspended and cultured in Matrigel with medium
388 (Advanced DMEM/F12 supplemented with penicillin/streptomycin, 10 mM HEPES, Glutamax,
389 13N2, 13B27 (all from Invitrogen), and 1mM N-acetylcysteine (Sigma) containing growth
390 factors 50 ng mL^{-1} EGF, 100 ng mL^{-1} noggin, 1mg mL^{-1} R-spondin). The organoid formation was
391 observed and analyzed every day after plating.

392

393 **METHOD DETAILS**

394 **Expression Plasmids, Viruses, Reagents, and Antibodies**

395 Expression plasmids encoding Flag-, Myc-, or HA-tagged wild-type or mutations of human
396 TBK1, IRF3, and the reporters of IFNβ_Luc and 5xISRE_Luc have been described previously
397 [78,79]. Flag- or HA-tagged human AMPKα1, AMPKα2, caAMPKα1 and AMPKα1 kinase domains
398 were constructed using the pRK5 mammalian expression vector. Site-directed mutagenesis
399 about TBK1 S511A/D/E and AMPKα1 T172D were generated by PCR-based cloning performed
400 by a kit from Stratagene. All coding sequences were verified by DNA sequencing, and the
401 detailed information for construction was provided in the attached Supplementary Table 2
402 and upon requirement.

403 The pharmacological reagent, Compound C (Selleck), AICAR (Selleck), 991 (Selleck), A-
404 769662 (Selleck), ABT-737 (Selleck), qVD-OPH (Selleck), S63845 (Selleck), MK2206 (Selleck),

405 Doxycycline (Sangon Biotech), 2-DG (Sangon Biotech), cGAMP (Invivogen), poly(I:C)
406 (Invivogen), poly (dA:dT) (Invivogen), puromycin (Yeasen), G418 (Yeasen), Hydroxyurea (HU)
407 (Sigma), and Lonidamine (Selleck) were purchased and used according to manual instructions.
408 Aldometanib was generated by Dr. Sheng-Cai Lin (Xiamen University, Xiamen).
409 The monoclonal anti-TBK1 (3504S, 1:5,000 dilution), anti-pTBK1(S172) (5483S, 1:3,000
410 dilution), anti-IRF3 (4302S, 1:2,000 dilution), anti-pIRF3 (S396) (4947S, 1:5,000 dilution), anti-
411 AMPKα (5831S, 1:1,000 dilution), anti-pAMPKα (T172) (50081S, 1:1,000 dilution), anti-pACC
412 (S79) (3661S, 1:1,000 dilution), anti-ACC (3676S, 1:1,000 dilution), anti-Myc (2276S, 1:3,000
413 dilution), and anti-HA (3724S, 1:5,000 dilution) antibodies were purchased from Cell Signaling
414 Technology. The anti-pIRF3 (S386) (ab76493, 1:3,000 dilution), anti-STING (ab181125, 1:100
415 dilution) were purchased from Abcam, and the anti-α-tubulin (T6199, 1:10,000 dilution), anti-
416 β-actin (A5441, 1:10,000 dilution), anti-GAPDH (EPR16891, 1:3000), anti-HA (H9658, 1:200
417 dilution), and anti-Flag (M2) (F3165, 1:5,000 dilution) were purchased from Sigma. The anti-
418 rabbit IgG and anti-mouse IgG antibodies were purchased from Santa Cruz. The anti-pTBK1
419 (S511) was generated in collaboration with Abcam, targeting the phospho-TBK1 S511.
420

421 **Plasmids Transfection and Virus Infection of Cultured Cells**

422 Lipofectamine 3000 (Invitrogen), Polyethyleneimine (PEI, Polysciences), or Lipofectamine
423 RNAiMAX (Invitrogen) transfection reagents were used for the transfection of plasmids,
424 poly(dA:dT), and poly(I:C). Digitonin (Sigma) was used to induce cGAMP.

425

426 **CRISPR/Cas9-mediated Generation of AMPKα1/α2$^{-/-}$ and TBK1 Knock-in Cells**

427 Guide RNA sequences targeting AMPKα1 and α2 mRNA sequence (hAMPKα1, 5'-
428 AAAGTTTGAGTGCTCAGAAG -3', 5'- GTGATGGAATATGTCTCAGG -3'; hAMPKα2, 5'-
429 TCAATTAACAGGCCATAAAG -3', 5'- GTTATTTAAGAAGATCCGAG -3'), TBK1 S511A/D knock-in
430 mRNA sequence (hTBK1, 5'- TATTTAGCTTTCCAGTTCTC -3', 5'- TTCTATTGTTCCCTGAGAAC -3')
431 were used to clone the genes into the vector pX330, which were transfected into DLD1 cells
432 by LipofectAmine 3000, together with the pCas9-2A-GFP plasmid, or with pCas9-2A-GFP and
433 pMD18 in the case of TBK1 S511A/D knock-in generation. 36 hours after transfection, cells

434 with green fluorescence were sorted with a Flow Cytometer (BD FACS Aria II) and propagated.
435 Immunoblotting with anti-AMPK(or the sequencing of the genomic PCR products) identified
436 clones. All gRNAs used in the experiments were also attached in Supplementary Table 1.
437
438 **Luciferase Reporter Assay**
439 HEK293 cells were transfected with indicated reporters (100 ng) bearing an open read frame
440 (ORF) coding Firefly luciferase, along with the pRL-Luc with Renilla luciferase coding as the
441 internal control for transfection and other expression vectors specified in the results section.
442 In brief, after 24 hours post-transfection, cells were lysed by passive lysis buffer (Promega),
443 and luciferase assays were performed using a dual luciferase assay kit (Promega), quantified
444 with POLARstar Omega (BMG Labtech) and normalized to the internal Renilla luciferase
445 control.
446
447 **Quantitative RT-PCR Assay**
448 The DLD1 cells stimulated with Hydroxyurea (HU), Camptothecin (CPT), or Etoposide (ETO)
449 were lysed, and total RNA was extracted using an RNAeasy extraction kit (Axygen). cDNA was
450 generated by a one-step iScript cDNA synthesis kit (Vazyme), and quantitative real-time PCR
451 was performed using the EvaGreen Qpcr MasterMix (Abm) and CFX96 real-time PCR system
452 (Bio-Rad). Relative quantification was expressed as 2-ΔCt, where Ct is the difference between
453 the primary Ct value of triplicates of the sample and an endogenous L19 mRNA control. The
454 primer sequences used are listed in the following:
455 hIL-1α, 5'- AGTGCTGCTGAAGGAGATGCCTGA -3', 5'- CCCCTGCCAAGCACACCCAGTA -3';
456 hIL-1β, 5'- ATGATGGCTTATTACAGTGGCAA -3', 5'- GTCGGAGATTCGTAGCTGGA -3';
457 RPL19, 5'- ATGTATCACAGCCTGTACCTG -3', 5'- TTCTTGGTCTCTTCCTCCTTG -3';
458 All primers used in the qRT-PCR assay were also attached in Supplementary Table 1.
459
460 **Coimmunoprecipitations and Immunoblottings**
461 HEK293 transfected with specified plasmids encoding Myc-, Flag-, or HA-tagged AMPKα1,
462 AMPKα2, TBK1s, and IRF3s was lysed using the modified MLB lysis buffer (20 mM Tris-Cl, 200

463 mM NaCl, 10 mM NaF, 1 mM NaV_2O_4, 1% NP-40, 20 mM β-glycerophosphate, and protease
464 inhibitor, pH 7.5) [31]. Cell lysates were then subjected to immunoprecipitation using the
465 antibodies of anti-Flag (Sigma, F3165-5MG, 1:200 dilution), anti-Myc (CST, 2276S, 1:200
466 dilution), or anti-HA (Sigma, H9658, 1:200 dilution) for transfected or induced proteins. After
467 3-4 washes with the MLB, adsorbed proteins were resolved by SDS-PAGE (Bio-Rad) and
468 immunoblotting with the indicated antibodies. Cell lysates were also analyzed using SDS-PAGE
469 and immunoblotting to control the protein abundance.
470
471 ***In vitro* Kinase Assay**
472 HEK293 cells were transfected with plasmids encoding Flag-, Myc-, or HA-tagged TBK1s or
473 AMPKα and lysed by the modified MLB lysis buffer after 24 hours of transfection.
474 Immunoprecipitations were performed by using anti-Flag (Sigma, F3165-5MG, 1:200 dilution),
475 anti-Myc (2276S, 1:200 dilution), or anti-HA (CST, 3724S, 1:200 dilution) antibodies. With two
476 washes by the MLB and two washes by the kinase assay buffer (200 μM ATP, 200 μM AMP, 20
477 mM Tris-HCl, 1 mM EGTA, 5 mM $MgCl_2$, 0.02% 2-mercapto-Ethanol, 0.03% Brij-35, and 0.2 mg
478 mL^{-1} BSA, PH 7.4), immunoprecipitated TBK1s and AMPKα1 were incubated in the kinase assay
479 buffer at 30°C for 60 min on THERMO-SHAKER (1400 rpm/min). The reaction was stopped by
480 adding 2 × SDS loading buffer and subjected to SDS-PAGE and specified immunoblotting.
481
482 **Cellular senescence assays**
483 To evaluate damage-induced cellular senescence, cells at approximately 60-70% confluence
484 were treated with Hydroxyurea (HU, 10 mM), Camptothecin (CPT, 1 μM), Etoposide (ETO, 25
485 μM) or Mitomycin (MMC, 1 μM) for 24 hours, replaced with fresh medium, and cultured for
486 another 5 days and harvested for SA-β-Gal assay, by using a cellular senescence assay kit
487 (Yeasen 40754ES60) and according to the manufacturer's manual. Images were acquired
488 using a converted fluorescence microscope from Nikon. , cells were lysed after 5-8 days
489 stimulations and subjected to RNA extraction and qRT-PCR assays as described in the previous
490 section, to detect the senescence-associated secretory phenotype (SASPs), such as the
491 expression of cytokines including IL-1α and IL-1β.

492 **Senescence assays in zebrafish**

493 Zebrafish embryos were treated with 50 nM CPT with/without 1mM AICAR or 10 μM
494 Compound C from 1.5 days post fertilization (dpf) to 3.5 dpf and then fixed in 4%
495 paraformaldehyde in PBS at 4°C. After 3 washes with PBS (pH 7.4 and pH 6.0) at 4°C, SA-β-Gal
496 staining was performed according to the manual of the senescence assay kit (Yeasen
497 40754ES60). Animals were photographed under a dissecting microscope.

498

499 **Murine allograft growth of B16 melanoma**

500 C57BL/6 wild-type mice were maintained under specific-pathogen-free (SPF) conditions and
501 randomly selected for tumor injection. Six- to eight-week-old mice were administered a
502 subcutaneous injection of 1.5×10^6 B16-F10 melanoma cells and treated with or without AICAR
503 (5 mg/kg) or once a day, Aldometanib was supplied either through oral gavaging[54]. From the
504 ninth-day post-tumor inoculation, the injected mice were monitored for tumor growth daily
505 as described in the protocols approved by the IACUC of Zhejiang University. Other treatment
506 regimens included: cGAMP, 2 μg intratumoral injection every 3 days, starting on day 5 post-
507 implantation; Lonidamine, 25 mg/kg intraperitoneal injection every 3 days, starting on day 4
508 post-implantation. Tumor size is presented as a square caliper measurement and was
509 calculated based on two perpendicular diameters (mm^2). The maximum diameter of tumors
510 is limited up to 10 mm by ethical permission, upon which the mice were sacrificed and
511 considered as dead due to tumor burden.

512

513 **Murine tumor Immunohistochemistry**

514 For immunohistochemistry assays, tumor samples were dissected, fixed in 4%
515 paraformaldehyde for 12 hours at 4°C, dehydrated with 30% sucrose overnight at 4°C,
516 embedded in optimal cutting temperature compound, and immediately frozen at -80°C. The
517 sectioned samples at 10 μm thickness were washed two times with PBS, permeabilized with
518 0.5% Triton X-100, blocked in 3% horse serum in PBS for 30 min, and incubated sequentially
519 with primary antibodies, including anti-CD3 (Abcam, 16669, 1:100 dilution), anti-CD4
520 (eBioscience, 14976680, 1:100 dilution), anti-CD8 (eBioscience, 14080880, 1:100 dilution),
521 and anti-F4/80 (Bio-Rad, MCA497RT, 1:100 dilution). After the sections were incubated with

522 Alexa-labeled secondary antibodies (Jackson, 111-095-003, 1:500 dilutions, Invitrogen,
523 A11006, 1:1000 dilutions) and extensively washed, they were stained with DAPI (Santa Cruz
524 Biotech) and mounted with ProLong™ Gold antifade reagent (Invitrogen).
525 Immunofluorescence images were obtained and analyzed using a Zeiss LSM710 or LSM 880
526 confocal microscope.
527

528 **Nano-liquid Chromatography/Tandem MS (Nano LC-MS/MS) Analysis**

529 Phoenix National Proteomics Core services performed Nano LC/tandem MS analysis for
530 protein identification and characterization and label-free quantification. Tryptic peptides were
531 separated on a C18 column and analyzed by LTQ-Orbitrap Velos (Thermo). Proteins were
532 identified using the National Center for Biotechnology Information search engine against the
533 human or mouse RefSeq protein databases. The mass spectrometry proteomics data of TBK1
534 modifications by AMPK have been deposited to the ProteomeXchange Consortium
535 (http://proteomecentral.proteomexchange.org) via the iProX partner repository with the
536 dataset identifier PXD033926.
537

538 **QUANTIFICATION AND STATISTICAL ANALYSIS**

539 Quantitative data are presented as the mean ± standard error of the mean (SEM) from at least
540 three independent experiments. When appropriate, the statistically significant differences
541 between multiple comparisons were analyzed using the one-way or two-way ANOVA test with
542 Bonferroni correction. Differences were considered significant at $p<0.05$. All samples were
543 included in the analyses if preserved and properly processed, and no samples or animals were
544 excluded except for zebrafish with conventional injection damage. No statistical method was
545 used to predetermine sample size, and all experiments except those involving animals were
546 not randomized. Immunoblotting, reporter assays, and qRT-PCR experiments have been
547 repeated a minimum of three times independently to ensure reproducibility. The investigators
548 were not blinded to allocation during experiments and outcome assessment.
549
550

551 **REFERENCES**

552 1 De Martino, M., Rathmell, J. C., Galluzzi, L. & Vanpouille-Box, C. Cancer cell metabolism and antitumour
553 immunity. *Nat Rev Immunol* **24**, 654-669 (2024). https://doi.org/10.1038/s41577-024-01026-4
554 2 Zhang, Q. *et al.* AMPK directly phosphorylates TBK1 to integrate glucose sensing into innate immunity.
555 *Mol Cell* **82**, 4519-4536 e4517 (2022). https://doi.org/10.1016/j.molcel.2022.10.026
556 3 Kao, K. C., Vilbois, S., Tsai, C. H. & Ho, P. C. Metabolic communication in the tumour-immune
557 microenvironment. *Nat Cell Biol* **24**, 1574-1583 (2022). https://doi.org/10.1038/s41556-022-01002-x
558 4 Hamanaka, R. B. & Chandel, N. S. Targeting glucose metabolism for cancer therapy. *J Exp Med* **209**, 211-
559 215 (2012). https://doi.org/10.1084/jem.20120162
560 5 Galluzzi, L., Kepp, O., Vander Heiden, M. G. & Kroemer, G. Metabolic targets for cancer therapy. *Nat Rev*
561 *Drug Discov* **12**, 829-846 (2013). https://doi.org/10.1038/nrd4145
562 6 Hay, N. Reprogramming glucose metabolism in cancer: can it be exploited for cancer therapy? *Nat Rev*
563 *Cancer* **16**, 635-649 (2016). https://doi.org/10.1038/nrc.2016.77
564 7 Roers, A., Hiller, B. & Hornung, V. Recognition of Endogenous Nucleic Acids by the Innate Immune
565 System. *Immunity* **44**, 739-754 (2016). https://doi.org/10.1016/j.immuni.2016.04.002
566 8 Chen, Q., Sun, L. & Chen, Z. J. Regulation and function of the cGAS-STING pathway of cytosolic DNA
567 sensing. *Nat Immunol* **17**, 1142-1149 (2016). https://doi.org/ni.3558 [pii]
568 10.1038/ni.3558
569 9 Chan, Y. K. & Gack, M. U. RIG-I-like receptor regulation in virus infection and immunity. *Curr Opin Virol*
570 **12**, 7-14 (2015). https://doi.org/S1879-6257(15)00005-X [pii]
571 10.1016/j.coviro.2015.01.004
572 10 Takeuchi, O. & Akira, S. Pattern recognition receptors and inflammation. *Cell* **140**, 805-820 (2010).
573 https://doi.org/10.1016/j.cell.2010.01.022
574 11 Zhang, Q., Chen, C., Xia, B. & Xu, P. Chemical regulation of the cGAS-STING pathway. *Curr Opin Chem*
575 *Biol* **69**, 102170 (2022). https://doi.org/10.1016/j.cbpa.2022.102170
576 12 Gao, P. *et al.* Cyclic [G(2',5')pA(3',5')p] is the metazoan second messenger produced by DNA-activated
577 cyclic GMP-AMP synthase. *Cell* **153**, 1094-1107 (2013). https://doi.org/10.1016/j.cell.2013.04.046
578 13 Sun, L., Wu, J., Du, F., Chen, X. & Chen, Z. J. Cyclic GMP-AMP synthase is a cytosolic DNA sensor that
579 activates the type I interferon pathway. *Science* **339**, 786-791 (2013).
580 https://doi.org/10.1126/science.1232458
581 14 Hu, M. M. & Shu, H. B. Innate Immune Response to Cytoplasmic DNA: Mechanisms and Diseases. *Annu*
582 *Rev Immunol* **38**, 79-98 (2020). https://doi.org/10.1146/annurev-immunol-070119-115052
583 15 Ablasser, A. *et al.* cGAS produces a 2'-5'-linked cyclic dinucleotide second messenger that activates
584 STING. *Nature* **498**, 380-384 (2013). https://doi.org/nature12306 [pii]
585 10.1038/nature12306
586 16 Wu, J. *et al.* Cyclic GMP-AMP is an endogenous second messenger in innate immune signaling by
587 cytosolic DNA. *Science* **339**, 826-830 (2013). https://doi.org/10.1126/science.1229963
588 17 Zhang, X. *et al.* Cyclic GMP-AMP containing mixed phosphodiester linkages is an endogenous high-
589 affinity ligand for STING. *Mol Cell* **51**, 226-235 (2013). https://doi.org/10.1016/j.molcel.2013.05.022
590 18 Ishikawa, H. & Barber, G. N. STING is an endoplasmic reticulum adaptor that facilitates innate immune
591 signalling. *Nature* **455**, 674-678 (2008). https://doi.org/10.1038/nature07317
592 19 Zhong, B. *et al.* The adaptor protein MITA links virus-sensing receptors to IRF3 transcription factor
593 activation. *Immunity* **29**, 538-550 (2008). https://doi.org/10.1016/j.immuni.2008.09.003
594 20 Sun, W. *et al.* ERIS, an endoplasmic reticulum IFN stimulator, activates innate immune signaling through

595 dimerization. *Proc Natl Acad Sci U S A* **106**, 8653-8658 (2009). https://doi.org/0900850106 [pii]
596 10.1073/pnas.0900850106
597 21 Zhang, D. *et al.* A non-canonical cGAS-STING-PERK pathway facilitates the translational program critical
598 for senescence and organ fibrosis. *Nat Cell Biol* **24**, 766-782 (2022). https://doi.org/10.1038/s41556-
599 022-00894-z
600 22 Gui, X. *et al.* Autophagy induction via STING trafficking is a primordial function of the cGAS pathway.
601 *Nature* **567**, 262-266 (2019). https://doi.org/10.1038/s41586-019-1006-9
602 23 Liu, S. *et al.* Phosphorylation of innate immune adaptor proteins MAVS, STING, and TRIF induces IRF3
603 activation. *Science* **347**, aaa2630 (2015). https://doi.org/10.1126/science.aaa2630
604 24 Zhang, C. *et al.* Structural basis of STING binding with and phosphorylation by TBK1. *Nature* **567**, 394-
605 398 (2019). https://doi.org/10.1038/s41586-019-1000-2
606 25 Sharma, S. *et al.* Triggering the interferon antiviral response through an IKK-related pathway. *Science*
607 **300**, 1148-1151 (2003). https://doi.org/10.1126/science.1081315
608 26 Fitzgerald, K. A. *et al.* IKKepsilon and TBK1 are essential components of the IRF3 signaling pathway. *Nat*
609 *Immunol* **4**, 491-496 (2003). https://doi.org/10.1038/ni921
610 27 Wild, P. *et al.* Phosphorylation of the autophagy receptor optineurin restricts Salmonella growth.
611 *Science* **333**, 228-233 (2011). https://doi.org/10.1126/science.1205405
612 28 Pilli, M. *et al.* TBK-1 promotes autophagy-mediated antimicrobial defense by controlling
613 autophagosome maturation. *Immunity* **37**, 223-234 (2012).
614 https://doi.org/10.1016/j.immuni.2012.04.015
615 29 Meng, F. *et al.* Induced phase separation of mutant NF2 imprisons the cGAS-STING machinery to
616 abrogate antitumor immunity. *Mol Cell* **81**, 4147-4164 e4147 (2021).
617 https://doi.org/10.1016/j.molcel.2021.07.040
618 30 Chen, S. *et al.* TBK1-Mediated DRP1 Targeting Confers Nucleic Acid Sensing to Reprogram Mitochondrial
619 Dynamics and Physiology. *Mol Cell* **80**, 810-827 e817 (2020).
620 https://doi.org/10.1016/j.molcel.2020.10.018
621 31 Xu, P. *et al.* Innate antiviral host defense attenuates TGF-beta function through IRF3-mediated
622 suppression of Smad signaling. *Mol Cell* **56**, 723-737 (2014).
623 https://doi.org/10.1016/j.molcel.2014.11.027
624 32 Dou, Z. *et al.* Cytoplasmic chromatin triggers inflammation in senescence and cancer. *Nature* **550**, 402-
625 406 (2017). https://doi.org/10.1038/nature24050
626 33 Yang, H., Wang, H., Ren, J., Chen, Q. & Chen, Z. J. cGAS is essential for cellular senescence. *Proc Natl*
627 *Acad Sci U S A* **114**, E4612-E4620 (2017). https://doi.org/10.1073/pnas.1705499114
628 34 Gluck, S. *et al.* Innate immune sensing of cytosolic chromatin fragments through cGAS promotes
629 senescence. *Nat Cell Biol* **19**, 1061-1070 (2017). https://doi.org/10.1038/ncb3586
630 35 Mackenzie, K. J. *et al.* cGAS surveillance of micronuclei links genome instability to innate immunity.
631 *Nature* **548**, 461-465 (2017). https://doi.org/10.1038/nature23449
632 36 Petrasek, J. *et al.* STING-IRF3 pathway links endoplasmic reticulum stress with hepatocyte apoptosis in
633 early alcoholic liver disease. *Proc Natl Acad Sci U S A* **110**, 16544-16549 (2013).
634 https://doi.org/10.1073/pnas.1308331110
635 37 Cerboni, S. *et al.* Intrinsic antiproliferative activity of the innate sensor STING in T lymphocytes. *J Exp*
636 *Med* **214**, 1769-1785 (2017). https://doi.org/jem.20161674 [pii]
637 10.1084/jem.20161674
638 38 Melki, I. *et al.* Disease-associated mutations identify a novel region in human STING necessary for the

639 control of type I interferon signaling. *J Allergy Clin Immunol* **140**, 543-552 e545 (2017).
640 https://doi.org/S0091-6749(16)31438-5 [pii]
641 10.1016/j.jaci.2016.10.031
642 39 Samson, N. & Ablasser, A. The cGAS-STING pathway and cancer. *Nat Cancer* **3**, 1452-1463 (2022).
643 https://doi.org/10.1038/s43018-022-00468-w
644 40 Chin, E. N., Sulpizio, A. & Lairson, L. L. Targeting STING to promote antitumor immunity. *Trends Cell Biol*
645 (2022). https://doi.org/10.1016/j.tcb.2022.06.010
646 41 Kwon, J. & Bakhoum, S. F. The Cytosolic DNA-Sensing cGAS-STING Pathway in Cancer. *Cancer Discov* **10**,
647 26-39 (2020). https://doi.org/10.1158/2159-8290.CD-19-0761
648 42 Chen, C. & Xu, P. Cellular functions of cGAS-STING signaling. *Trends Cell Biol* **33**, 630-648 (2023).
649 https://doi.org/10.1016/j.tcb.2022.11.001
650 43 Bakhoum, S. F. *et al.* Chromosomal instability drives metastasis through a cytosolic DNA response.
651 *Nature* **553**, 467-472 (2018). https://doi.org/10.1038/nature25432
652 44 Chen, Q. *et al.* Carcinoma-astrocyte gap junctions promote brain metastasis by cGAMP transfer. *Nature*
653 **533**, 493-498 (2016). https://doi.org/10.1038/nature18268
654 45 Hong, C. *et al.* cGAS-STING drives the IL-6-dependent survival of chromosomally instable cancers.
655 *Nature* **607**, 366-373 (2022). https://doi.org/10.1038/s41586-022-04847-2
656 46 Li, S. *et al.* STING-induced regulatory B cells compromise NK function in cancer immunity. *Nature* **610**,
657 373-380 (2022). https://doi.org/10.1038/s41586-022-05254-3
658 47 Concepcion, A. R. *et al.* The volume-regulated anion channel LRRC8C suppresses T cell function by
659 regulating cyclic dinucleotide transport and STING-p53 signaling. *Nat Immunol* **23**, 287-302 (2022).
660 https://doi.org/10.1038/s41590-021-01105-x
661 48 Zhou, R. *et al.* TBK1-Zyxin signaling controls tumor-associated macrophage recruitment to mitigate
662 antitumor immunity. *EMBO J* **43**, 4984-5017 (2024). https://doi.org/10.1038/s44318-024-00244-9
663 49 Hardie, D. G. & Ashford, M. L. AMPK: regulating energy balance at the cellular and whole body levels.
664 *Physiology (Bethesda)* **29**, 99-107 (2014). https://doi.org/10.1152/physiol.00050.2013
665 50 Hardie, D. G., Ross, F. A. & Hawley, S. A. AMPK: a nutrient and energy sensor that maintains energy
666 homeostasis. *Nat Rev Mol Cell Biol* **13**, 251-262 (2012). https://doi.org/10.1038/nrm3311
667 51 Lin, S. C. & Hardie, D. G. AMPK: Sensing Glucose as well as Cellular Energy Status. *Cell Metab* **27**, 299-
668 313 (2018). https://doi.org/10.1016/j.cmet.2017.10.009
669 52 Zhang, C. S. *et al.* The lysosomal v-ATPase-Ragulator complex is a common activator for AMPK and
670 mTORC1, acting as a switch between catabolism and anabolism. *Cell Metab* **20**, 526-540 (2014).
671 https://doi.org/10.1016/j.cmet.2014.06.014
672 53 Zhang, C. S. *et al.* Fructose-1,6-bisphosphate and aldolase mediate glucose sensing by AMPK. *Nature*
673 **548**, 112-116 (2017). https://doi.org/10.1038/nature23275
674 54 Zhang, C. S. *et al.* The aldolase inhibitor aldometanib mimics glucose starvation to activate lysosomal
675 AMPK. *Nat Metab* **4**, 1369-1401 (2022). https://doi.org/10.1038/s42255-022-00640-7
676 55 Garcia, D. & Shaw, R. J. AMPK: Mechanisms of Cellular Energy Sensing and Restoration of Metabolic
677 Balance. *Mol Cell* **66**, 789-800 (2017). https://doi.org/10.1016/j.molcel.2017.05.032
678 56 Gonzalez, A., Hall, M. N., Lin, S. C. & Hardie, D. G. AMPK and TOR: The Yin and Yang of Cellular Nutrient
679 Sensing and Growth Control. *Cell Metab* **31**, 472-492 (2020).
680 https://doi.org/10.1016/j.cmet.2020.01.015
681 57 Mouchiroud, L., Eichner, L. J., Shaw, R. J. & Auwerx, J. Transcriptional coregulators: fine-tuning
682 metabolism. *Cell Metab* **20**, 26-40 (2014). https://doi.org/10.1016/j.cmet.2014.03.027

683 58 Zhao, P. *et al.* TBK1 at the Crossroads of Inflammation and Energy Homeostasis in Adipose Tissue. *Cell*
684 **172**, 731-743 e712 (2018). https://doi.org/10.1016/j.cell.2018.01.007
685 59 Klil-Drori, A. J., Azoulay, L. & Pollak, M. N. Cancer, obesity, diabetes, and antidiabetic drugs: is the fog
686 clearing? *Nat Rev Clin Oncol* **14**, 85-99 (2017). https://doi.org/10.1038/nrclinonc.2016.120
687 60 Rodrigues Mantuano, N. *et al.* Hyperglycemia Enhances Cancer Immune Evasion by Inducing Alternative
688 Macrophage Polarization through Increased O-GlcNAcylation. *Cancer Immunol Res* **8**, 1262-1272 (2020).
689 https://doi.org/10.1158/2326-6066.CIR-19-0904
690 61 Incio, J. *et al.* Obesity-Induced Inflammation and Desmoplasia Promote Pancreatic Cancer Progression
691 and Resistance to Chemotherapy. *Cancer Discov* **6**, 852-869 (2016). https://doi.org/10.1158/2159-
692 8290.CD-15-1177
693 62 Clements, V. K. *et al.* Frontline Science: High fat diet and leptin promote tumor progression by inducing
694 myeloid-derived suppressor cells. *J Leukoc Biol* **103**, 395-407 (2018).
695 https://doi.org/10.1002/JLB.4HI0517-210R
696 63 Keerthana, C. K. *et al.* The role of AMPK in cancer metabolism and its impact on the immunomodulation
697 of the tumor microenvironment. *Front Immunol* **14**, 1114582 (2023).
698 https://doi.org/10.3389/fimmu.2023.1114582
699 64 Reinfeld, B. I. *et al.* Cell-programmed nutrient partitioning in the tumour microenvironment. *Nature* **593**,
700 282-288 (2021). https://doi.org/10.1038/s41586-021-03442-1
701 65 Ramakrishnan, G., Terry, A. R., Nogueira, V., Magdy, A. & Hay, N. Deletion of AMP-activated protein
702 kinase impairs metastasis and is rescued by ROS scavenging or ectopic CD36 expression. *Cell Rep* **44**,
703 115183 (2025). https://doi.org/10.1016/j.celrep.2024.115183
704 66 Corton, J. M., Gillespie, J. G., Hawley, S. A. & Hardie, D. G. 5-aminoimidazole-4-carboxamide
705 ribonucleoside. A specific method for activating AMP-activated protein kinase in intact cells? *Eur J*
706 *Biochem* **229**, 558-565 (1995). https://doi.org/10.1111/j.1432-1033.1995.tb20498.x
707 67 McArthur, K. *et al.* BAK/BAX macropores facilitate mitochondrial herniation and mtDNA efflux during
708 apoptosis. *Science* **359** (2018). https://doi.org/10.1126/science.aao6047
709 68 Rongvaux, A. *et al.* Apoptotic caspases prevent the induction of type I interferons by mitochondrial DNA.
710 *Cell* **159**, 1563-1577 (2014). https://doi.org/10.1016/j.cell.2014.11.037
711 69 White, M. J. *et al.* Apoptotic caspases suppress mtDNA-induced STING-mediated type I IFN production.
712 *Cell* **159**, 1549-1562 (2014). https://doi.org/10.1016/j.cell.2014.11.036
713 70 Chiappinelli, K. B. *et al.* Inhibiting DNA Methylation Causes an Interferon Response in Cancer via dsRNA
714 Including Endogenous Retroviruses. *Cell* **162**, 974-986 (2015).
715 https://doi.org/10.1016/j.cell.2015.07.011
716 71 Sasaki, N. *et al.* RNA sensing induced by chromosome missegregation augments antitumor immunity.
717 *Mol Cell* (2024). https://doi.org/10.1016/j.molcel.2024.11.025
718 72 Gulen, M. F. *et al.* Signalling strength determines proapoptotic functions of STING. *Nat Commun* **8**, 427
719 (2017). https://doi.org/10.1038/s41467-017-00573-w
720 73 Wu, S. *et al.* HER2 recruits AKT1 to disrupt STING signalling and suppress antiviral defence and
721 antitumour immunity. *Nat Cell Biol* **21**, 1027-1040 (2019). https://doi.org/10.1038/s41556-019-0352-z
722 74 Floridi, A. *et al.* Lonidamine, a selective inhibitor of aerobic glycolysis of murine tumor cells. *J Natl*
723 *Cancer Inst* **66**, 497-499 (1981).
724 75 Roberts, D. J., Tan-Sah, V. P., Ding, E. Y., Smith, J. M. & Miyamoto, S. Hexokinase-II positively regulates
725 glucose starvation-induced autophagy through TORC1 inhibition. *Mol Cell* **53**, 521-533 (2014).
726 https://doi.org/10.1016/j.molcel.2013.12.019

727 76 Wu, Y. Q. *et al.* Low glucose metabolite 3-phosphoglycerate switches PHGDH from serine synthesis to
728 p53 activation to control cell fate. *Cell Res* **33**, 835-850 (2023). https://doi.org/10.1038/s41422-023-
729 00874-4
730 77 Ghosh, M. *et al.* Mutant p53 suppresses innate immune signaling to promote tumorigenesis. *Cancer Cell*
731 **39**, 494-508 e495 (2021). https://doi.org/10.1016/j.ccell.2021.01.003
732 78 Zhang, Q. *et al.* Hippo signalling governs cytosolic nucleic acid sensing through YAP/TAZ-mediated TBK1
733 blockade. *Nat Cell Biol* **19**, 362-374 (2017). https://doi.org/10.1038/ncb3496
734 79 Liu, S. *et al.* Lck/Hck/Fgr-Mediated Tyrosine Phosphorylation Negatively Regulates TBK1 to Restrain
735 Innate Antiviral Responses. *Cell Host Microbe* **21**, 754-768 e755 (2017).
736 https://doi.org/10.1016/j.chom.2017.05.010
737
738

739 **FIGURE LEGENDS**

740 **Figure 1. Glucose deficiency promotes intratumoral cGAS-STING signaling. (A-B)**, The
741 intratumoral glucose deficiency state in B16-F10 melanoma was validated through
742 immunofluorescence of phospho-ACC1 (pACC), a primary substrate of AMPK, by which an
743 evident signal of pACC was seen in the edge of melanoma (A). AMPK agonist AICAR treatment
744 was set as the positive control (B). Scale bars=50 µm**. (C-E),** Cytosolic dsDNA sensing was
745 evaluated in PMs (C), MEFs (D), and DLD1 (E) under 2-DG or AICAR (AMPK agonist)
746 administration in response to STING agonist cGAMP, as indicated by immunoblotting using
747 antibodies recognizing active forms of TBK1 and IRF3. **(F-G)**, Sensing of mtDNAs, released
748 upon the treatment of ABT-737, qVD-OPH, and S63845 (AQS), was similarly augmented by
749 glucose depletion, revealed by the phosphorylation level of TBK1. **(H)**, The effects of AICAR
750 administration on TpdAdT-induced DNA sensing were evaluated in DLD1, representing
751 enhanced dsDNA sensing to double-stranded DNA. ***Applied to figures 1-6***: unless specified,
752 n=3 independent experiments (mean±SEM); *, P<0.05, **, P<0.01, and ***, P<0.001, by
753 statistical analysis of the indicated comparison with ANOVA and Bonferroni correction.

754

755 **Figure 2. AMPK facilitates cGAS-STING signaling in cancer cells by TBK1 S511**
756 **phosphorylation. (A)**, Double knockout (dKO) of AMPK α1 and α2 impaired the activation of
757 TBK1 and IRF3 following DMXAA stimulation in B16-F10 melanoma cells. **(B)**, The genetic
758 ablation of AMPK α1 and α2 subunits reduced TpIC-induced cytosolic RNA sensing in HCT116,
759 revealed by a significant decrease in phosphorylation of TBK1 and IRF3. **(C)**,
760 Coimmunoprecipitation assay revealed coexpression of AMPKα1 or caAMPKα1 (activated
761 AMPKα1) enhanced this association of TBK1 and IRF3 2SA. **(D)**, Reporter assay showed that
762 the expression of AMPK α1 and α2 subunits strongly promoted TBK1-stimulated IRF3
763 transactivation with IFNβ promoter in HEK293 cells. **(E)**, Mass spectrometry analysis identified
764 that AMPKα1 phosphorylated the S511 residue of TBK1, and the phosphorylation was
765 completely inhibited by the AMPK inhibitor dorsomorphin (Compound C). **(F)**, caAMPKα1 and
766 AMPKa1 kinase domain directly phosphorylated TBK1 at S511 in vitro kinase assay. **(G-H)**,
767 TBK1 mutants S511A (resistant to AMPK modification) exhibited significantly reduced activity
768 IRF3-responsive reporter assays (G) and a weaker interaction with IRF3 2SA (H). Meanwhile,

769 TBK1 S511E (mimics AMPK-phosphorylated TBK1) demonstrated a strong potential to bind
770 and activate IRF3. **(I-J)**, Generated DLD1 knock-in (KI) clones with mutations that either
771 prevent (S511A) or mimic (S511D) AMPK-mediated modification using CRISPR-based genome
772 editing. cGAMP-stimulated cGAS-STING pathway was weakened in TBK1 S511A KI cells (I) but
773 strengthened in S511D KI cells (J).
774
775 **Figure 3. AMPK drives STING-induced senescence and apoptosis of cancer cells and**
776 **organoids. (A-B)**, Chemical induction of DNA damage in DLD1 gut epithelial cells by CPT,
777 mitomycin C (MMC), etoposide (ETO), and hydroxyurea (HU) treatment led to a robust
778 phenotype of cellular senescence, as assessed by SA-β-Gal staining (A) and SASP features,
779 including the mRNA expression of IL1α and IL1β (B). Genetic ablation of AMPKα1/α2 in DLD1
780 cells prevented DNA sensing-initiated cellular senescence (A). Conversely, AICAR treatment
781 significantly enhanced DNA damage-induced cellular senescence (B). Scale bars = 100 µm. **(C)**,
782 Energy deficiency stimulation of AMPK by 2-DG or AICAR led to an exaggerated phenotype of
783 cellular senescence in DLD1 cells, particularly upon HU-induced DNA damage. Scale bars = 100
784 µm. ***, P<0.001, by ANOVA with Bonferroni correction. **(D)**, Cellular senescence was
785 assessed in zebrafish embryos (n=30) subjected to chemical-induced damage by incubation
786 with CPT (50 nM) and to SA-β-Gal staining. A strong phenotype of cellular senescence was
787 detected in the heads and tails of zebrafish; this phenotype was mildly upregulated by AICAR
788 treatment but was mitigated by dorsomorphin. Scale bars = 500 µm. **(E)**, FACS analyses of early
789 and late apoptotic cells among DLD1 cells revealed that activation of AMPK by AICAR
790 promoted cell apoptosis induced by cytosolic DNA sensing, which triggered by DNA damage
791 inducer HU, but inhibition of AMPK by dorsomorphin suppressed HU-induced apoptosis. **(F)**,
792 Intestinal crypts were isolated from mice at 6 weeks of age and cultured *in vitro* in the absence
793 or presence of the AMPK agonist AICAR. PI staining revealed that cytosolic DNA sensing
794 stimulated by the DNA damage inducer HU resulted in robust apoptosis of intestinal cells in
795 organoids, and AICAR exaggerated this effect. Scale bars=50 µm. n=15 intestinal organoids
796 examined (mean±SEM). *, P=0.002, compared with wild-type organoids (ANOVA with
797 Bonferroni correction).
798

799 **Figure 4. AMPK-TBK1 signaling facilitates STING-mediated antitumor immunity in**
800 **melanomas. (A-C)**, The STING SAVI mutant (R281Q) was constitutively active (caSTING). The
801 volumes (A), weights (B), and photos (C) of the subcutaneously B16-F10 melanoma growth in
802 wild-type C57BL/6 mice revealed a markedly decreased growth in melanomas expressing the
803 STING SAVI mutant (R281Q). AICAR administration further increased this effect of STING
804 signaling, resulting in robust tumor growth arrest. n=12 inoculations per group (mean ± SEM),
805 measured 7 days post tumor inoculation (dpti). **(D-E)**, The administration of AICAR with
806 caSTING profoundly increased immune cell infiltration, particularly the infiltration of the $CD4^+$
807 and $CD8^+$ T cells into melanomas, as detected by Immunohistochemistry (IHC) upon STING
808 SAVI mutant expression (D). The statistics for the immunohistochemistry-positive cells were
809 calculated (E). Scale bars=20 µm. **, P<0.01, and ***, P<0.001, by ANOVA with Bonferroni
810 correction. **(F-H)**, B16-F10 melanoma cells were implanted subcutaneously into $TBK1^{WT/WT}$ or
811 $TBK1^{S511E/S511E}$ C57BL/6 mice with intratumoral injection of cGAMP. Volumes (F), weights (G),
812 and photos (H) of melanoma revealed that melanoma growth was markedly attenuated in
813 these $TBK1^{S511E/S511E}$ mice. **(I-J)**, Immunohistochemistry (I), and statistics (J) showed B16-F10
814 melanoma from $TBK1^{S511E/S511E}$ mice accompanied with the increased immune cell infiltration.
815 Stimulation in $TBK1^{S511E/S511E}$ mice by cGAMP did not further enhance the infiltrated T cells
816 and antitumor immunity effect. Scale bars=20 µm.
817
818 **Figure 5. AMPK agonists synergize well with cGAMP to promote antitumor immunity in**
819 **melanomas. (A-C)**, The weights (A), volumes (B), and photos (C) of the subcutaneously B16-
820 F10 melanoma growth in wild-type C57BL/6 mice with administration of cGAMP or AICAR.
821 AICAR administration further promoted the antitumor immunity effect of cGAMP-induced
822 STING signaling, inhibiting tumor growth. n=6 inoculations per group (mean ± SEM). **(D-F)**, The
823 weights (D), volumes (E), and photos (F) of the subcutaneously B16-F10 melanoma growth in
824 wild-type C57BL/6 mice with administration of Aldometanib and cGAMP. Adding AICAR
825 enhanced the suppression of tumor growth induced by cGAMP. n=4 inoculations per group
826 (mean ± SEM). **(G-I)**, Administration of Aldometanib alone inhibited the growth of AMPK dKO
827 B16-F10 tumors in WT mice. The weights (G), volumes (H), and photos (I) showed similar
828 tumor sizes of AMPK dKO B16-F10 tumors with the treatment of Aldometanib or cGAMP. n=8

829 inoculations per group (mean ± SEM).

830

831 **Figure 6. Disrupting aerobic glycolysis potentiates antitumor immunity through the AMPK-**
832 **TBK1 cascade.** The administration of Lonidamine (Hexokinase inhibitor) with cGAMP
833 profoundly inhibited the growth of B16-F10 melanoma, revealed by the volumes (D), weights
834 (E), and photos (F) of B16-F10 melanoma. (D) n=10 inoculations per group (mean ± SEM). (E)
835 n=8 inoculations per group (mean ± SEM). **(G-H)**, Enhanced infiltration of $CD3^+$, $CD4^+$, and $CD8^+$
836 T lymphocytes were imaged in B16-F10 tumors with the administration of Lonidamine and
837 cGAMP; Scale bars, 20 µm. (H) n=3 per group (mean ± SEM). **(I)**, Immunohistochemistry
838 showed that Lonidamine enhanced cGAMP-induced cGAS-STING signaling in tumors, as
839 evidenced by increased levels of phosphorylated STING (pSTING S365) and phosphorylated
840 TBK1 (pTBK1 S172) in B16-F10 melanomas; Scale bars=20 µm.

Figure 1

A

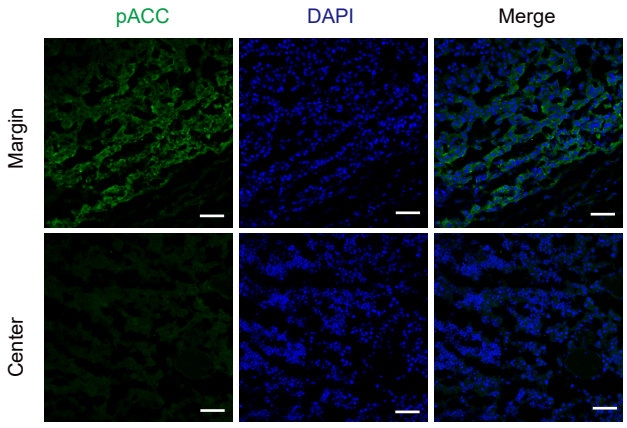

B16-F10 Tumor/DMSO

B

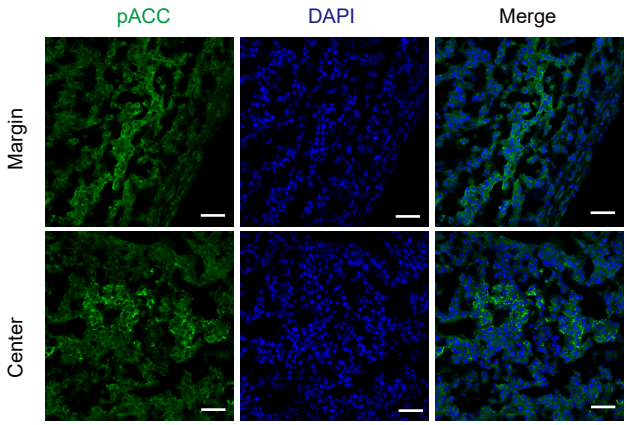

B16-F10 Tumor/AICAR

C

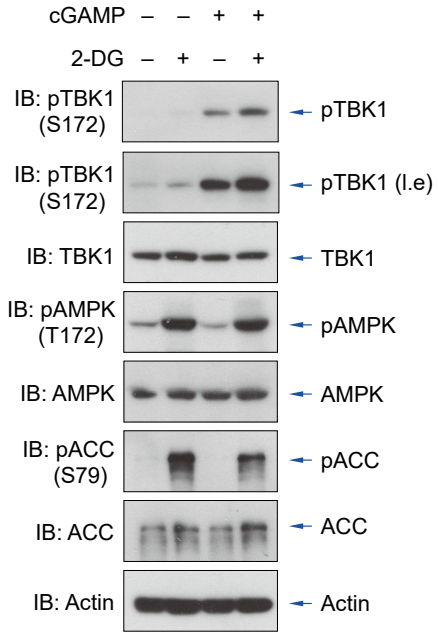

PMs

D

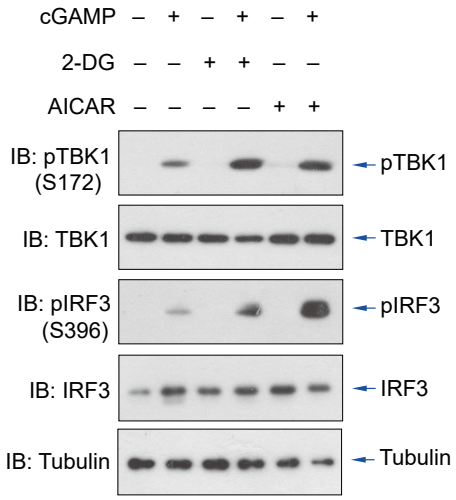

MEFs

E

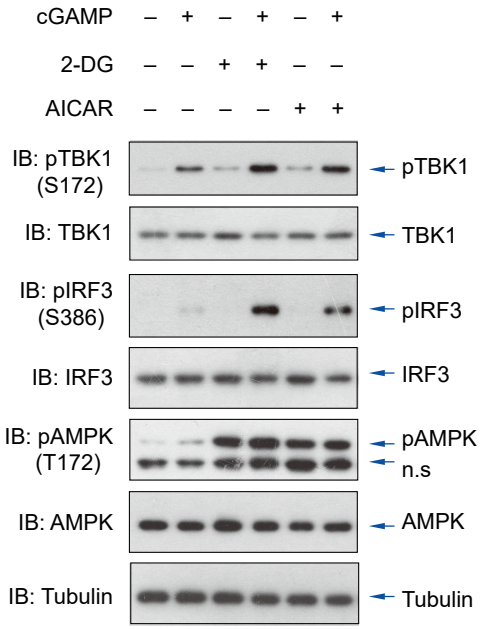

DLD1

F

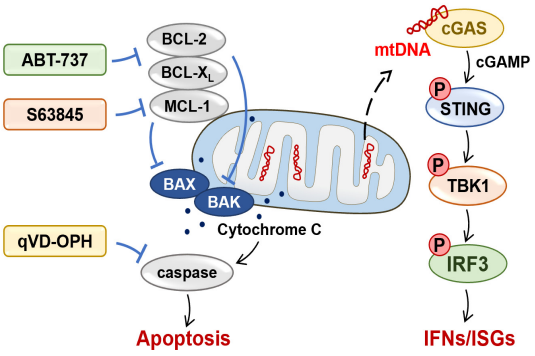

G

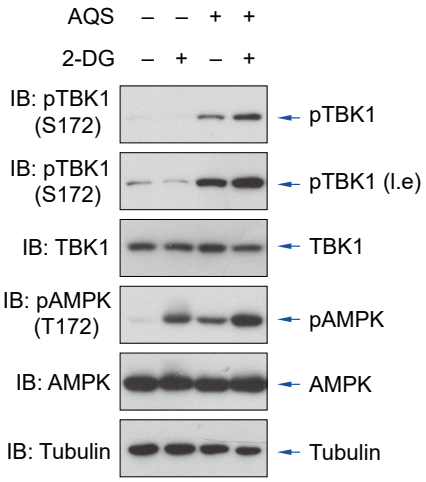

DLD1

H

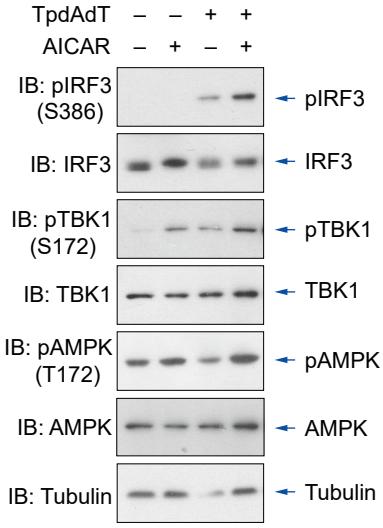

DLD1

Figure 2

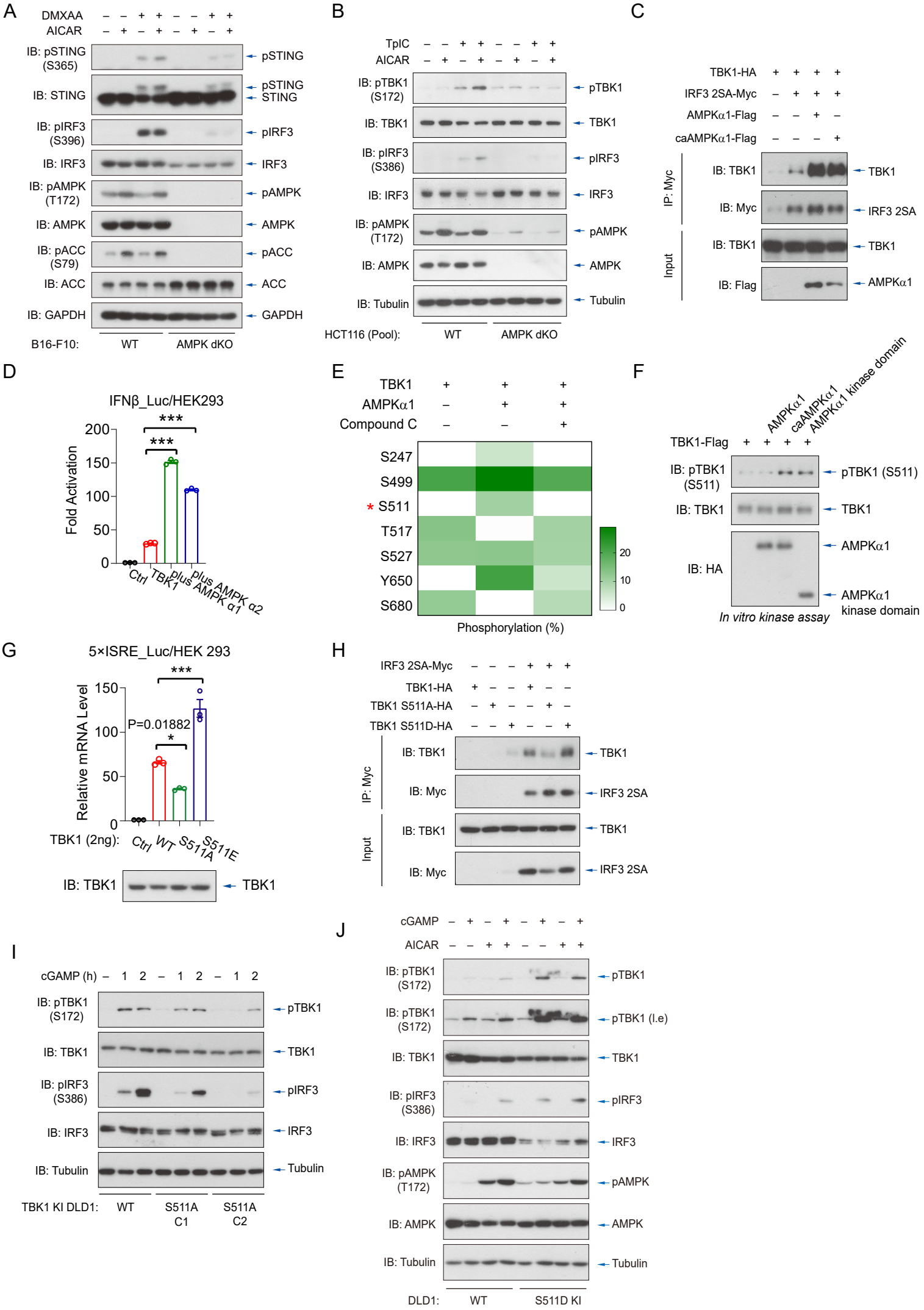
A
DMXAA
AICAR
IB: pSTING (S365)
IB: STING
IB: pIRF3 (S396)
IB: IRF3
IB: pAMPK (T172)
IB: AMPK
IB: pACC (S79)
IB: ACC
IB: GAPDH
pSTING
STING
pIRF3
IRF3
pAMPK
AMPK
pACC
ACC
GAPDH
B16-F10:
WT
AMPK dKO
B
TpIC
AICAR
IB: pTBK1 (S172)
IB: TBK1
IB: pIRF3 (S386)
IB: IRF3
IB: pAMPK (T172)
IB: AMPK
IB: Tubulin
pTBK1
TBK1
pIRF3
IRF3
pAMPK
AMPK
Tubulin
HCT116 (Pool):
WT
AMPK dKO
C
TBK1-HA
IRF3 2SA-Myc
AMPKα1-Flag
caAMPKα1-Flag
IP: Myc
Input
IB: TBK1
IB: Myc
IB: TBK1
IB: Flag
TBK1
IRF3 2SA
TBK1
AMPKα1
D
IFNβ_Luc/HEK293
Fold Activation
200
150
100
50
0
***
***
Ctrl
TBK1
plus AMPK α1
plus AMPK α2
E
TBK1
AMPKα1
Compound C
S247
S499
* S511
T517
S527
Y650
S680
20
10
0
Phosphorylation (%)
F
AMPKα1
caAMPKα1
AMPKα1 kinase domain
TBK1-Flag
IB: pTBK1 (S511)
IB: TBK1
IB: HA
pTBK1 (S511)
TBK1
AMPKα1
AMPKα1 kinase domain
In vitro kinase assay
G
5×ISRE_Luc/HEK 293
Relative mRNA Level
150
100
50
0
***
P=0.01882
*
TBK1 (2ng):
Ctrl
WT
S511A
S511E
IB: TBK1
TBK1
H
IRF3 2SA-Myc
TBK1-HA
TBK1 S511A-HA
TBK1 S511D-HA
IP: Myc
Input
IB: TBK1
IB: Myc
IB: TBK1
IB: Myc
TBK1
IRF3 2SA
TBK1
IRF3 2SA
I
cGAMP (h)
IB: pTBK1 (S172)
IB: TBK1
IB: pIRF3 (S386)
IB: IRF3
IB: Tubulin
pTBK1
TBK1
pIRF3
IRF3
Tubulin
TBK1 KI DLD1:
WT
S511A C1
S511A C2
J
cGAMP
AICAR
IB: pTBK1 (S172)
IB: pTBK1 (S172)
IB: TBK1
IB: pIRF3 (S386)
IB: IRF3
IB: pAMPK (T172)
IB: AMPK
IB: Tubulin
pTBK1
pTBK1 (l.e)
TBK1
pIRF3
IRF3
pAMPK
AMPK
Tubulin
DLD1:
WT
S511D KI

Figure 3

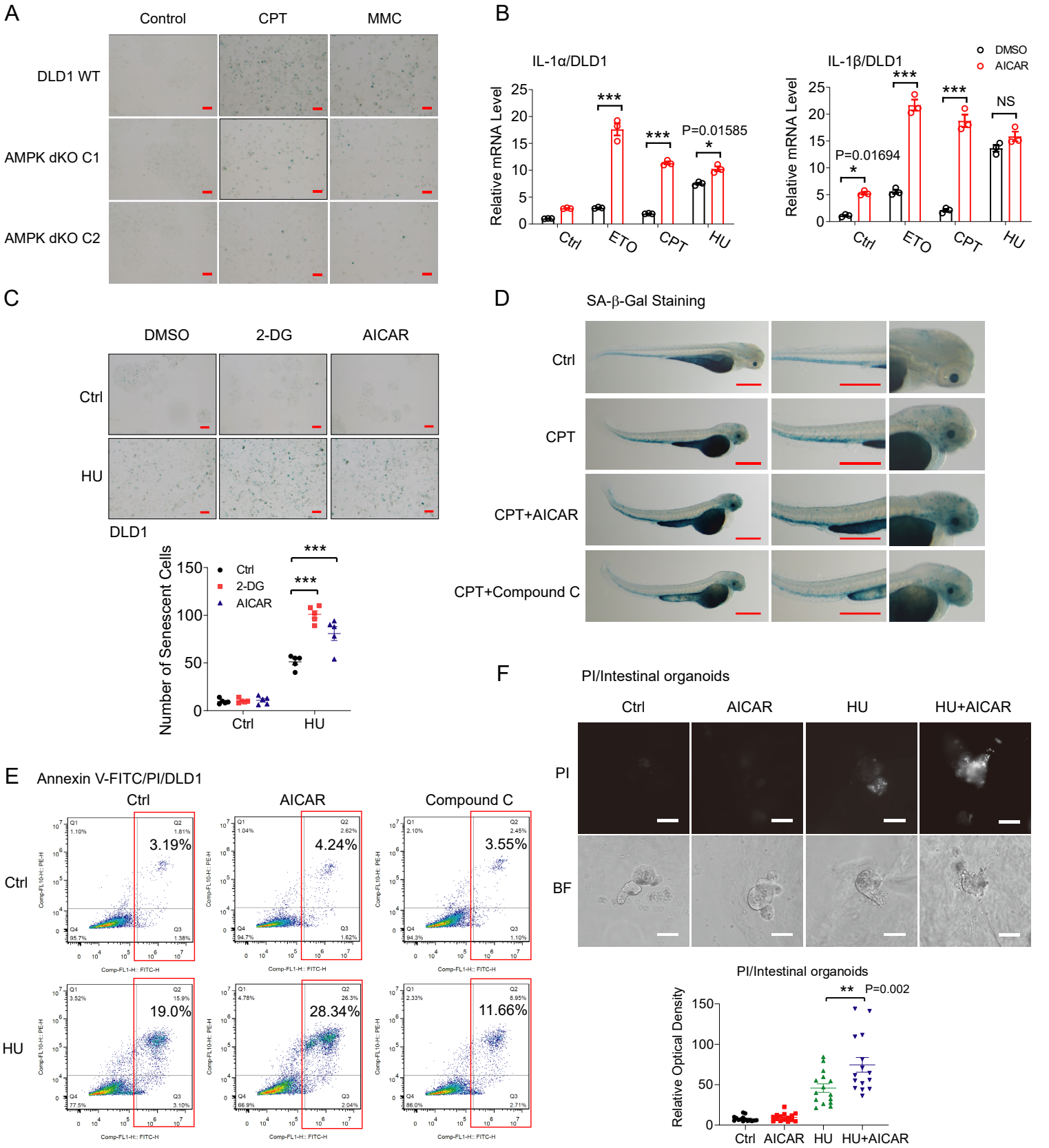
A
Control
CPT
MMC
DLD1 WT
AMPK dKO C1
AMPK dKO C2
B
IL-1α/DLD1
Relative mRNA Level
***
***
P=0.01585
*
Ctrl
ETO
CPT
HU
IL-1β/DLD1
DMSO
AICAR
P=0.01694
NS
C
DMSO
2-DG
AICAR
Ctrl
HU
DLD1
Number of Senescent Cells
Ctrl
2-DG
AICAR
D
SA-β-Gal Staining
Ctrl
CPT
CPT+AICAR
CPT+Compound C
E
Annexin V-FITC/PI/DLD1
Ctrl
AICAR
Compound C
3.19%
4.24%
3.55%
19.0%
28.34%
11.66%
F
PI/Intestinal organoids
Ctrl
AICAR
HU
HU+AICAR
PI
BF
PI/Intestinal organoids
Relative Optical Density
**
P=0.002

Figure 4

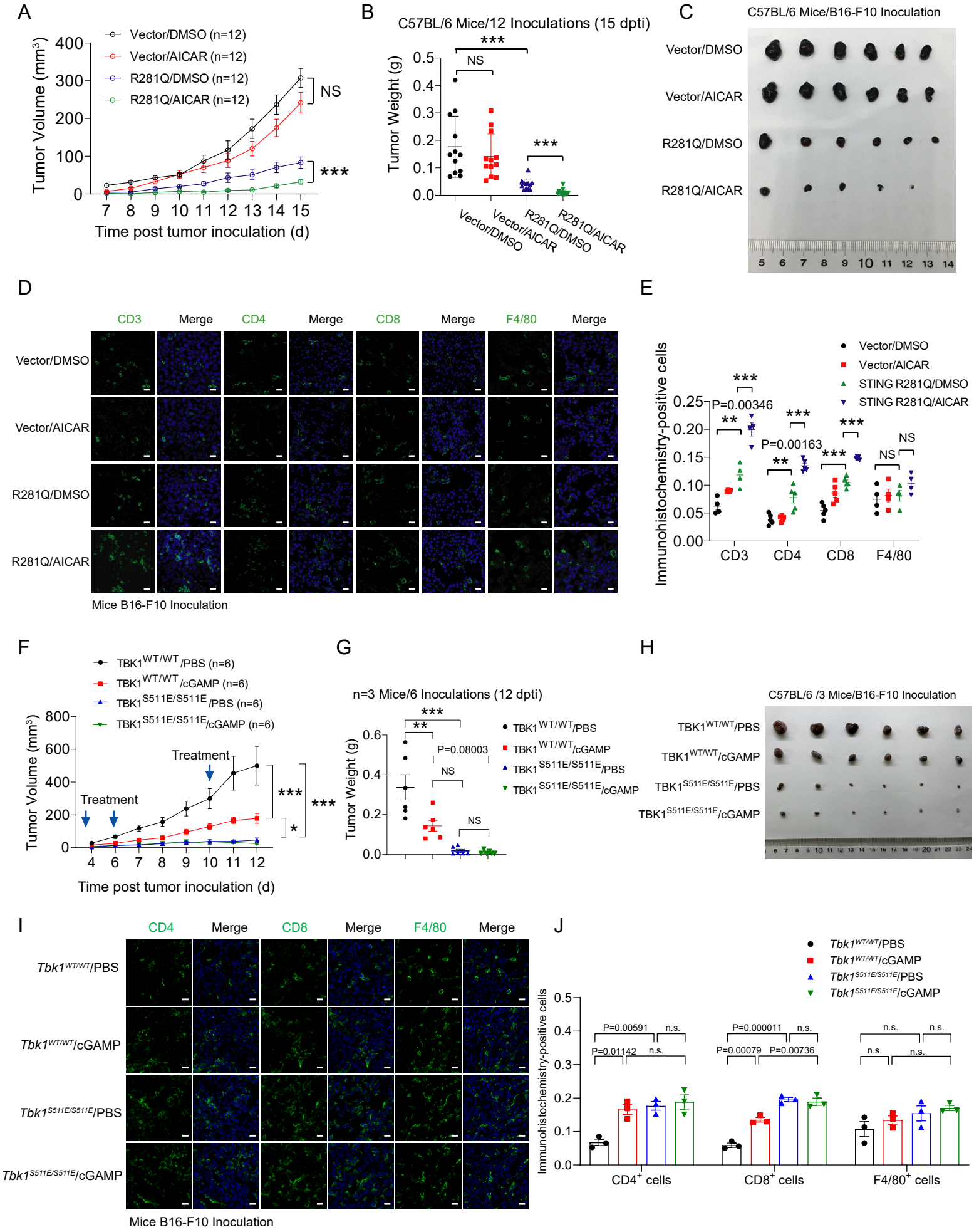
A
Vector/DMSO (n=12)
Vector/AICAR (n=12)
R281Q/DMSO (n=12)
R281Q/AICAR (n=12)
Tumor Volume (mm³)
Time post tumor inoculation (d)
NS
***
B
C57BL/6 Mice/12 Inoculations (15 dpti)
Tumor Weight (g)
Vector/DMSO
Vector/AICAR
R281Q/DMSO
R281Q/AICAR
C
C57BL/6 Mice/B16-F10 Inoculation
D
CD3
Merge
CD4
CD8
F4/80
Mice B16-F10 Inoculation
E
Immunohistochemistry-positive cells
STING R281Q/DMSO
STING R281Q/AICAR
P=0.00346
P=0.00163
F
TBK1WT/WT/PBS (n=6)
TBK1WT/WT/cGAMP (n=6)
TBK1S511E/S511E/PBS (n=6)
TBK1S511E/S511E/cGAMP (n=6)
Treatment
G
n=3 Mice/6 Inoculations (12 dpti)
P=0.08003
H
C57BL/6 /3 Mice/B16-F10 Inoculation
I
Tbk1WT/WT/PBS
Tbk1WT/WT/cGAMP
Tbk1S511E/S511E/PBS
Tbk1S511E/S511E/cGAMP
J
P=0.00591
P=0.01142
P=0.000011
P=0.00079
P=0.00736
n.s.
CD4+ cells
CD8+ cells
F4/80+ cells

Figure 5

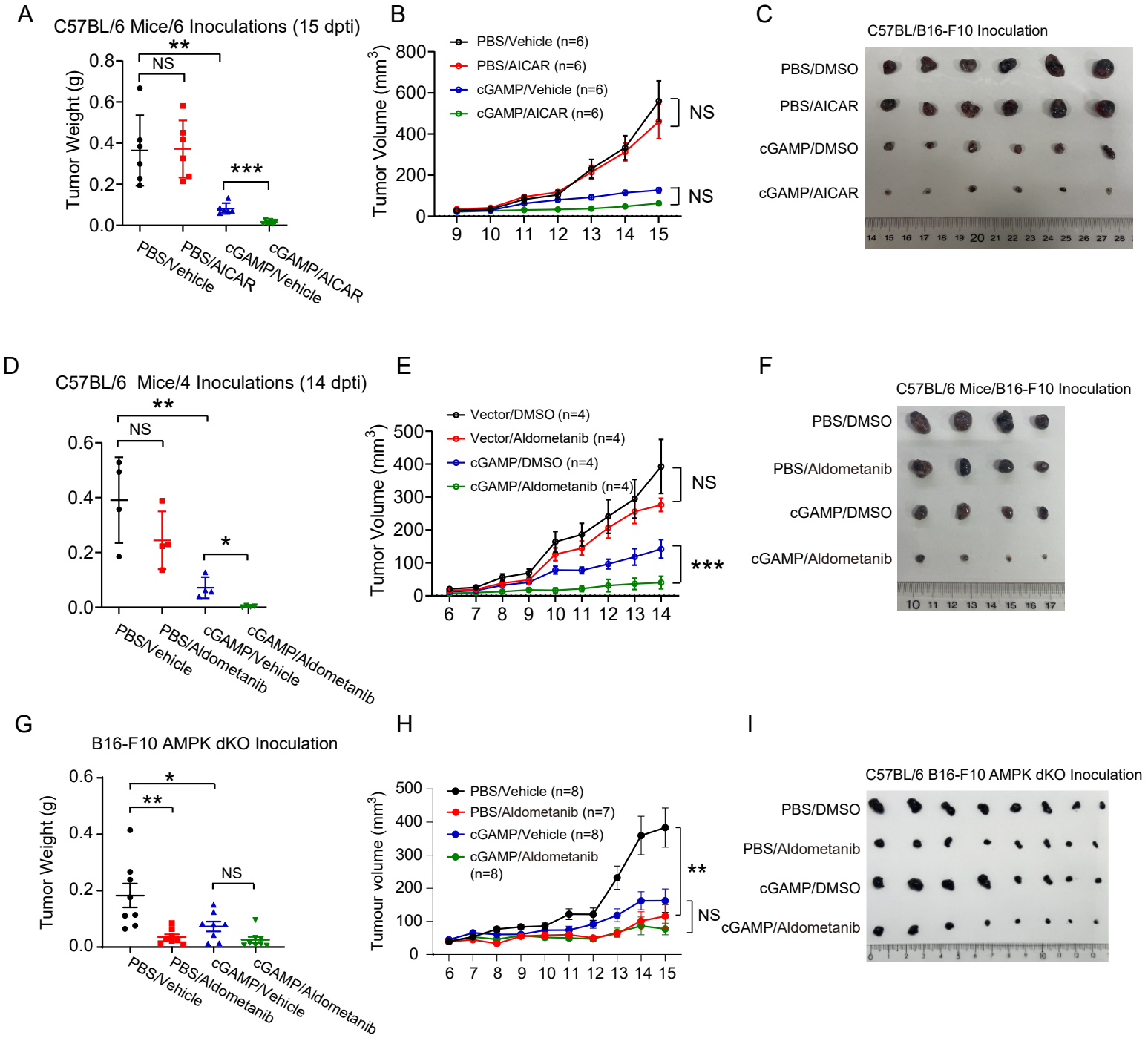
A
C57BL/6 Mice/6 Inoculations (15 dpti)
Tumor Weight (g)
0.8
0.6
0.4
0.2
0.0
**
NS
***
PBS/Vehicle
PBS/AICAR
cGAMP/Vehicle
cGAMP/AICAR
B
Tumor Volume (mm3)
800
600
400
200
0
PBS/Vehicle (n=6)
PBS/AICAR (n=6)
cGAMP/Vehicle (n=6)
cGAMP/AICAR (n=6)
NS
NS
9 10 11 12 13 14 15
C
C57BL/B16-F10 Inoculation
PBS/DMSO
PBS/AICAR
cGAMP/DMSO
cGAMP/AICAR
D
C57BL/6 Mice/4 Inoculations (14 dpti)
0.6
0.4
0.2
0.0
**
NS
*
PBS/Vehicle
PBS/Aldometanib
cGAMP/Vehicle
cGAMP/Aldometanib
E
Tumor Volume (mm3)
500
400
300
200
100
0
Vector/DMSO (n=4)
Vector/Aldometanib (n=4)
cGAMP/DMSO (n=4)
cGAMP/Aldometanib (n=4)
NS
***
6 7 8 9 10 11 12 13 14
F
C57BL/6 Mice/B16-F10 Inoculation
PBS/DMSO
PBS/Aldometanib
cGAMP/DMSO
cGAMP/Aldometanib
G
B16-F10 AMPK dKO Inoculation
Tumor Weight (g)
0.6
0.4
0.2
0.0
*
**
NS
PBS/Vehicle
PBS/Aldometanib
cGAMP/Vehicle
cGAMP/Aldometanib
H
Tumour volume (mm3)
500
400
300
200
100
0
PBS/Vehicle (n=8)
PBS/Aldometanib (n=7)
cGAMP/Vehicle (n=8)
cGAMP/Aldometanib (n=8)
**
NS
6 7 8 9 10 11 12 13 14 15
I
C57BL/6 B16-F10 AMPK dKO Inoculation
PBS/DMSO
PBS/Aldometanib
cGAMP/DMSO
cGAMP/Aldometanib

Figure 6

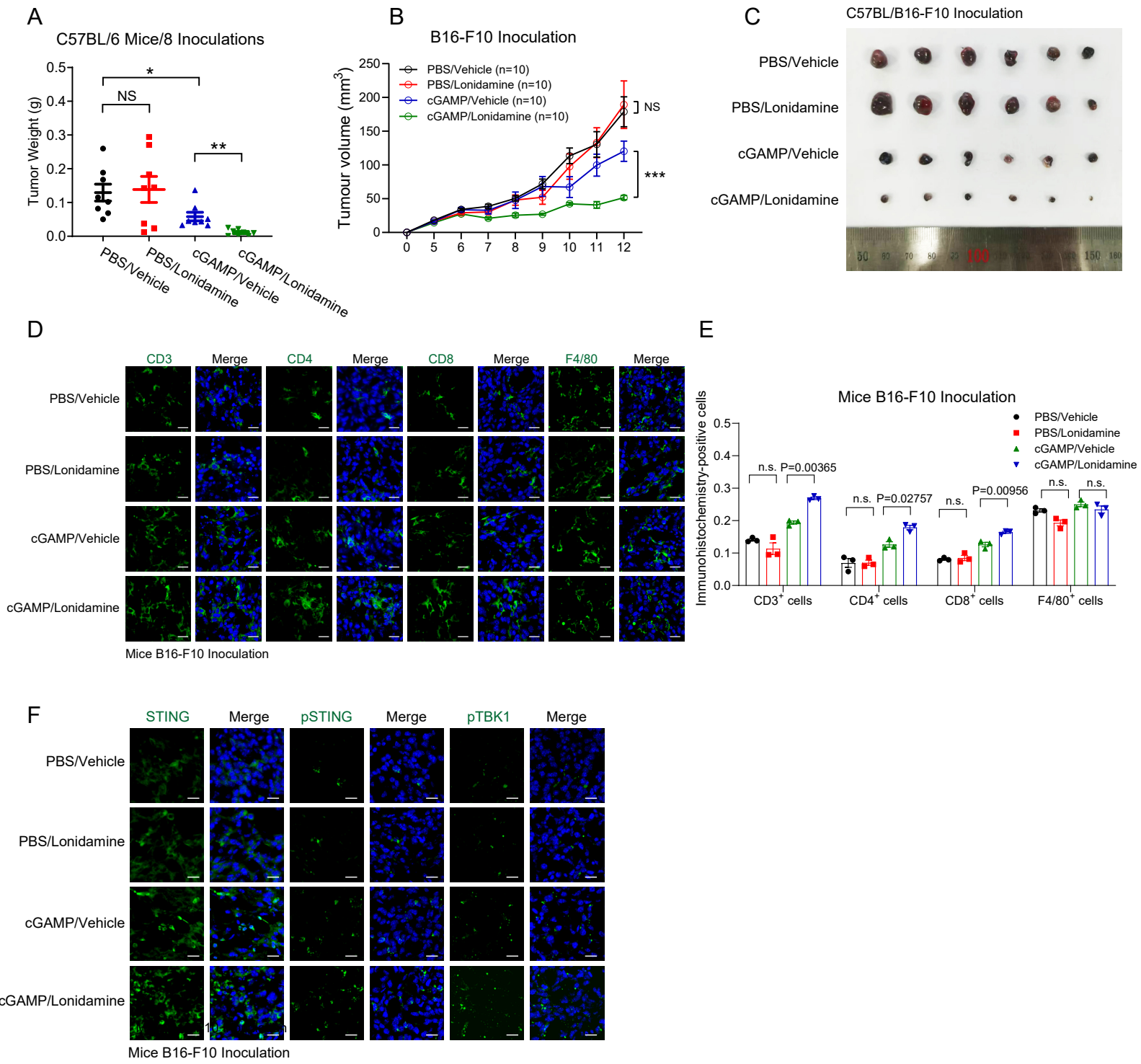
A
C57BL/6 Mice/8 Inoculations
Tumor Weight (g)
0.5
0.4
0.3
0.2
0.1
0.0
*
NS
**
PBS/Vehicle
PBS/Lonidamine
cGAMP/Vehicle
cGAMP/Lonidamine
B
B16-F10 Inoculation
Tumour volume (mm3)
250
200
150
100
50
0
PBS/Vehicle (n=10)
PBS/Lonidamine (n=10)
cGAMP/Vehicle (n=10)
cGAMP/Lonidamine (n=10)
NS
***
0 5 6 7 8 9 10 11 12
C
C57BL/B16-F10 Inoculation
PBS/Vehicle
PBS/Lonidamine
cGAMP/Vehicle
cGAMP/Lonidamine
D
CD3
Merge
CD4
Merge
CD8
Merge
F4/80
Merge
PBS/Vehicle
PBS/Lonidamine
cGAMP/Vehicle
cGAMP/Lonidamine
Mice B16-F10 Inoculation
E
Mice B16-F10 Inoculation
Immunohistochemistry-positive cells
0.5
0.4
0.3
0.2
0.1
0.0
PBS/Vehicle
PBS/Lonidamine
cGAMP/Vehicle
cGAMP/Lonidamine
n.s.
P=0.00365
n.s.
P=0.02757
n.s.
P=0.00956
n.s.
n.s.
CD3+ cells
CD4+ cells
CD8+ cells
F4/80+ cells
F
STING
Merge
pSTING
Merge
pTBK1
Merge
PBS/Vehicle
PBS/Lonidamine
cGAMP/Vehicle
cGAMP/Lonidamine
Mice B16-F10 Inoculation

Figure 1

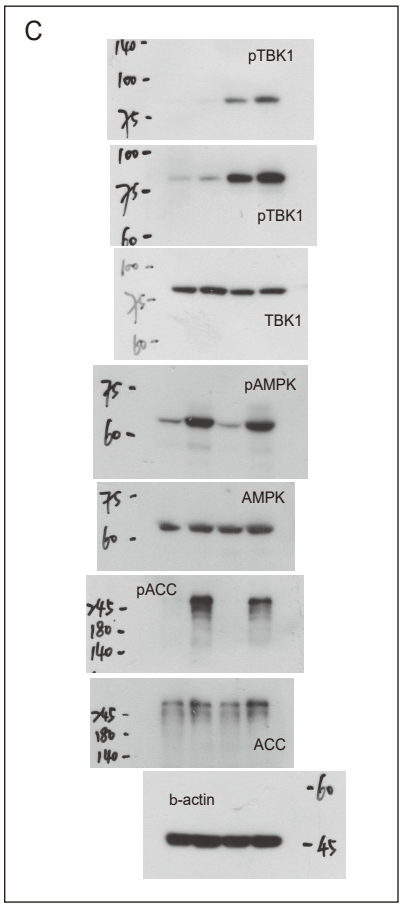

Figure 1

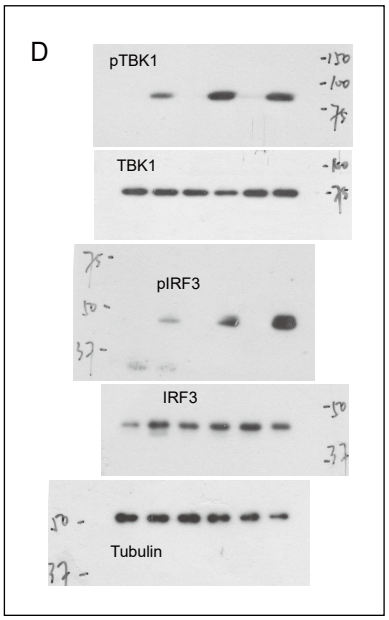

Figure 1

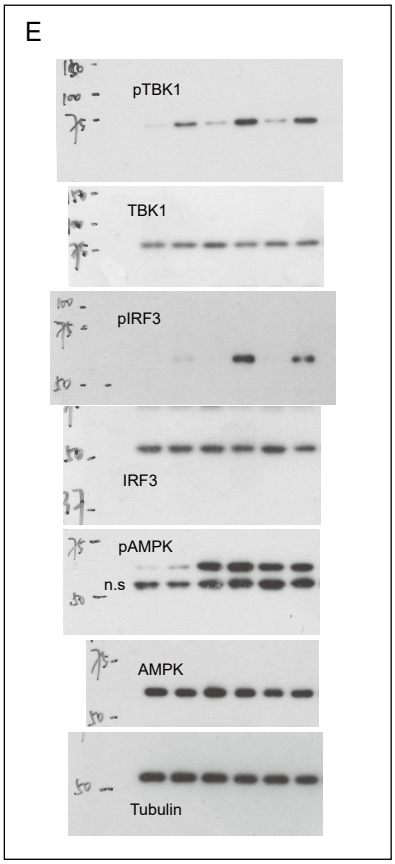

Figure 1

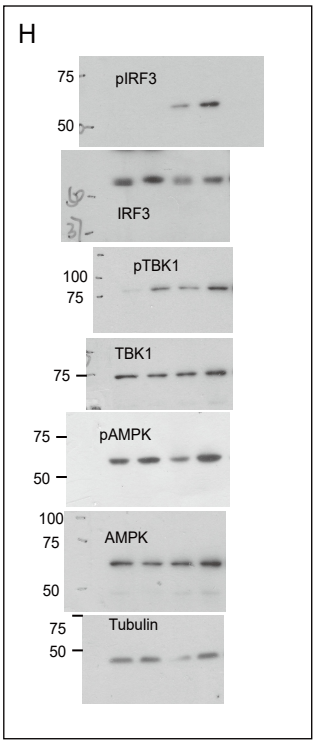

Figure 1

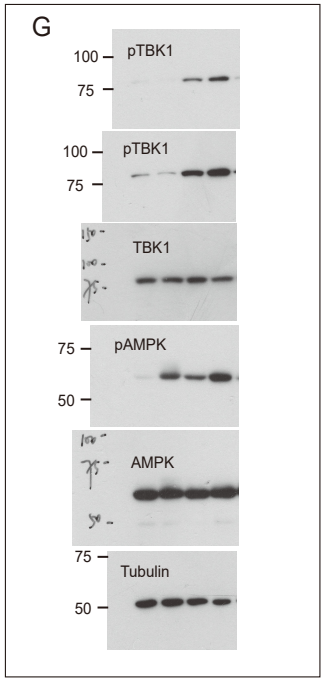

Figure 2

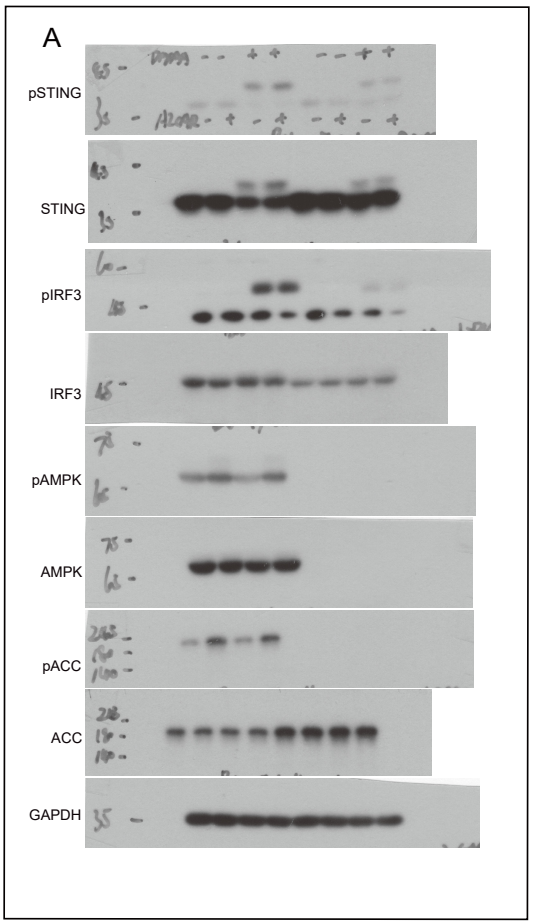

Figure 2

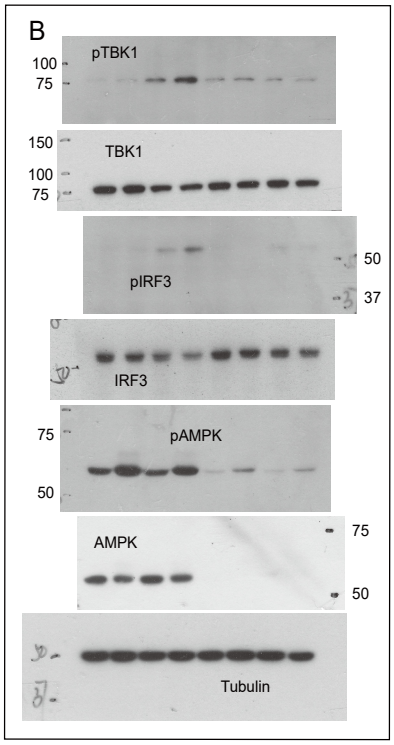

Figure 2

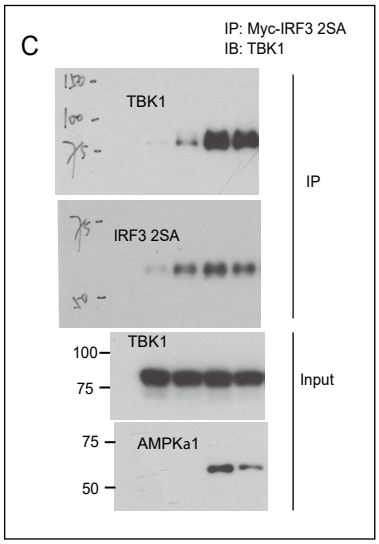

Figure 2

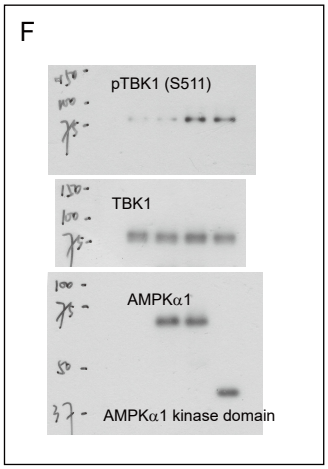

Figure 2

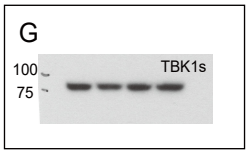

Figure 2

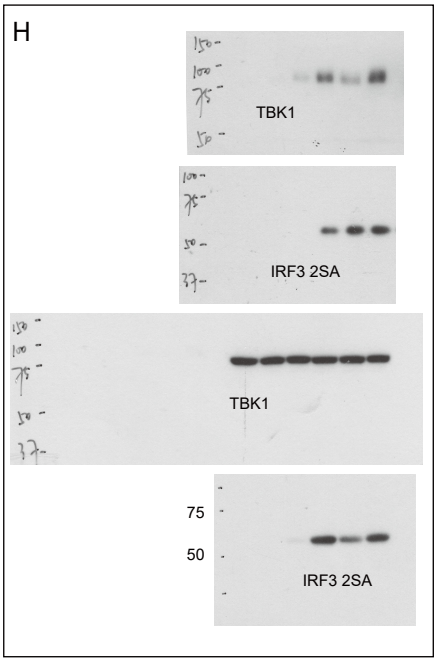

Figure 2

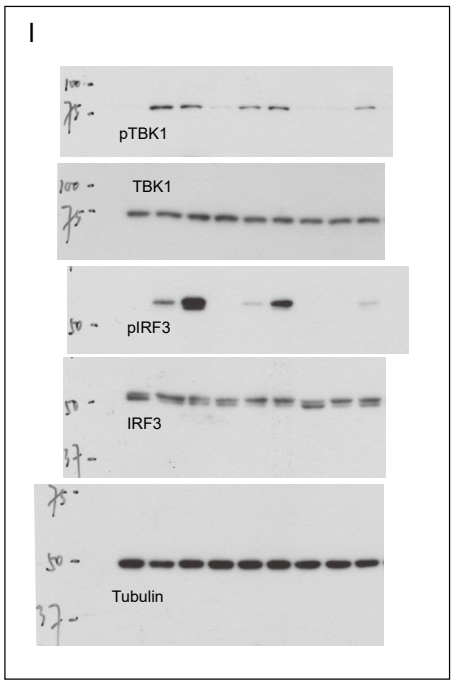

Figure 2

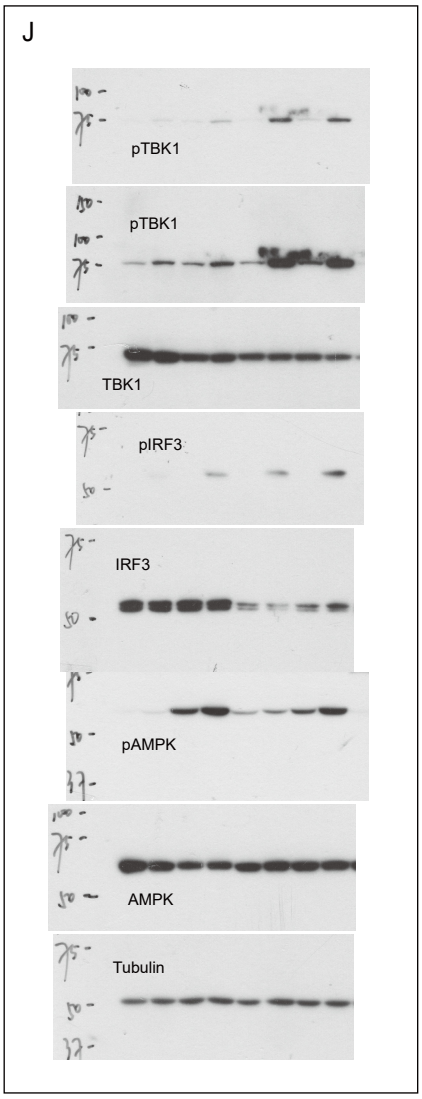

Suppl. Table 1_Oligos Used in Study

qPCR Primers	Sequence	Species	Company
IL-1a-Forward Primer	5' - AGTGCTGCTGAAGGAGATGCCTGA - 3'	human	biosune
IL-1a-Reverse Primer	5' - CCCCTGCCAAGCACACCCAGTA - 3'	human	biosune
IL-1b-Forward Primer	5' - ATGATGGCTTATTACAGTGGCAA - 3'	human	biosune
IL-1b-Reverse Primer	5' - GTCGGAGATTCGTAGCTGGA - 3'	human	biosune
RPL19-Forward Primer	5' - ATGTATCACAGCCTGTACCTG - 3'	human	biosune
RPL19-Reverse Primer	5' - TTCTTGGTCTCTTCCTCCTTG - 3'	human	biosune

Primers

Cas9 Primers	Sequence	Species	Company
AMPKα1-Cas9-Forward Primer	5' - CACCGAAAGTTTGAGTGCTCAGAAG - 3'	human	biosune
AMPKα1-Cas9-Reverse Primer	5' - AAACCTTCTGAGCACTCAAACTTTC - 3'	human	biosune
AMPKα2-Cas9-Forward Primer	5' - CACCGTCAATTAACAGGCCATAAAG - 3'	human	biosune
AMPKα2-Cas9-Reverse Primer	5' - AAACCTTTATGGCCTGTTAATTGAC - 3'	human	biosune
TBK1-S511A/D-Knock-In-Forward Primer	5' - CACCGTATTTAGCTTTCCAGTTCTC - 3'	human	biosune
TBK1-S511A/D-Knock-In-Reverse Primer	5' - AAACGAGAACTGGAAAGCTAAATAC - 3'	human	biosune

Suppl. Table 2_ List of Recombinant DNA

DNA	SOURCE	IDENTIFIER
pRK5-HA-TBK1 S511A	This paper	N/A
pRK5-HA-TBK1 S511D	This paper	N/A
pRK5-HA-TBK1 S511E	This paper	N/A
pRK5-Flag-TBK1 S511A	This paper	N/A
pRK5-Flag-TBK1 S511D	This paper	N/A
pRK5-Flag-TBK1 S511E	This paper	N/A
pRK5-HA-AMPKα1	This paper	N/A
pRK5-HA-AMPKα1 T172D	This paper	N/A
pRK5-HA-AMPKα1 kinase domain (1-312)	This paper	N/A
pRK5-Flag-AMPKα1	This paper	N/A
pRK5-Flag-TBK1	Lab stored	N/A
pRK5-HA-TBK1	Lab stored	N/A
pRK5-Myc-TBK1	Lab stored	N/A
pRK5-Myc-IRF3	Lab stored	N/A
pRK5-Myc-IRF3 2SA	Lab stored	N/A
pIFNβ_Luc	Lab stored	N/A
p5xISRE_Luc	Lab stored	N/A
gRNA	Lab stored	N/A
Cas9-2A-GFP	Lab stored	N/A
pMD18	Lab stored	N/A
pX330	Addgene	Cat#42230

Suppl. Table 3_Statistics Source Data
(See details in the following sheets)